prostacyclin receptor. *Nature.* 388:678–682.
21. Shinomiya, S., et al. 2001. Regulation of TNFα and interleukin-10 production by prostaglandins I_2 and E_2: studies with prostaglandin receptor-deficient mice and prostaglandin E-receptor subtype-selective synthetic agonists. *Biochem. Pharmacol.* 61:1153–1160.
22. Pujino, T., et al. 2002. Effects of the prostanoids on the proliferation or hypertrophy of cultured murine aortic smooth muscle cells. *Br. J. Pharmacol.* 136:530–539.
23. Hoshikwa, Y., et al. 2001. Prostacyclin receptor-dependent modulation of pulmonary vascular remodeling. *Am. J. Respir. Crit. Care. Med.* 164:314–318.
24. Xiao, C.Y., et al. 2001. Roles of prostaglandin I_2 and thromboxane A_2 in cardiac ischemia-reperfusion injury: a study using mice lacking their respective receptors. *Circulation.* 104:2210–2215.
25. Takahashi, Y., et al. 2002. Augmentation of allergic inflammation in prostanoid IP receptor deficient mice. *Br. J. Pharmacol.* 137:315–322.
26. Nagao, K., et al. 2003. Role of prostaglandin I_2 in airway remodeling induced by repeated allergen challenge in mice. *Am. J. Respir. Cell Mol. Biol.* 29:314–320.
27. Arai, K., et al. 2003. Endogenous prostaglandin I_2 regulates the neural emergency system through release of calcitonin gene related peptide. *Gut.* 52:1242–1249.
28. Yamada, T., et al. 2003. Thromboxane A_2 regulates vascular tone via its inhibitory effect on the expression of inducible nitric oxide synthase. *Circulation.* 108:2381–2386.
29. Katagiri, H., et al. 2004. Role of thromboxane derived from COX-1 and -2 in hepatic microcirculatory dysfunction during endotoxemia in mice. *Hepatology.* 39:139–150.
30. Rosenfeld, M.E., et al. 2000. Advanced atherosclerotic lesions in the innominate artery of the apoE knockout mouse. *Arterioscler. Thromb. Vasc. Biol.* 20:2587–2592.
31. Cheng, Y., et al. 2002. Role of prostacyclin in the cardiovascular response to thromboxane A_2. *Science.* 296:539–541.
32. Nakashima, Y., Plump, A.S., Raines, E.W., Breslow, J.L., and Ross, R. 1994. ApoE-deficient mice develop lesions of all phases of atherosclerosis throughout the arterial tree. *Arterioscler. Thromb.* 14:133–140.
33. Pratico, D., Cyrus, T., Li, H., and FitzGerald, G.A. 2000. Endogenous biosynthesis of thromboxane and prostacyclin in 2 distinct murine models of atherosclerosis. *Blood.* 96:3823–3826.
34. Libby, P., Schoenbeck, U., Mach, F., Selwyn, A.P., and Ganz, P. 1998. Current concepts in cardiovascular pathology: the role of LDL cholesterol in plaque rupture and stabilization. *Am. J. Med.* 104:14S–18S.
35. Hartung, H.P., Kladetzky, R.G., Melnik, B., and Hennerici, M. 1986. Stimulation of the scavenger receptor on monocytes-macrophages evokes release of arachidonic acid metabolites and reduced oxygen species. *Lab. Invest.* 55:209–216.
36. Fitzgerald, D.J., Roy, L., Catella, F., and FitzGerald, G.A. 1986. Platelet activation in unstable coronary disease. *N. Engl. J. Med.* 315:983–989.
37. Cipollone, F., et al. 2001. Overexpression of functionally coupled cyclooxygenase-2 and prostaglandin E synthase in symptomatic atherosclerotic plaques as a basis of prostaglandin E_2-dependent plaque instability. *Circulation.* 104:921–927.
38. Cipollone, F., et al. 2003. The receptor RAGE as a progression factor amplifying arachidonate-dependent inflammatory and proteolytic response in human atherosclerotic plaques: role of glycemic control. *Circulation.* 108:1070–1077.
39. Kitahara, M., et al. 2001. Prostacyclin inhibits the production of MMP-9 induced by phorbol ester through protein kinase A activation, but does not affect the production of MMP-2 in human cultured mesangial cells. *Kidney Blood Press. Res.* 24:18–26.
40. Schermuly, R. T., et al. 2004. Antiremodeling effects of iloprost and the dual-selective phosphodiesterase 3/4 inhibitor tolafentrine in chronic experimental pulmonary hypertension. *Circ. Res.* 94:1101–1108.
41. Trip, M.D., Cats, V.M., van Capelle, F.J., and Vreeken, J. 1990. Platelet hyperreactivity and prognosis in survivors of myocardial infarction. *N. Engl. J. Med.* 322:1549–1554.
42. van Zanten, G.H., et al. 1994. Increased platelet deposition on atherosclerotic coronary arteries. *J. Clin. Invest.* 93:615–632.
43. Broijersen, A., Hamsten, A., Eriksson, M., Angelin, B., and Hjemdahl, P. 1998. Platelet activity in vivo in hyperlipoproteinemia-importance of combined hyperlipidemia. *Thromb. Haemost.* 79:268–275.
44. Broijersen, A., Karpe, P., Hamsten, A., Goodall, A.H., and Hjemdahl, P. 1998. Alimentary lipemia enhances the membrane expression of platelet P-selectin without affecting other markers of platelet activation. *Atherosclerosis.* 137:107–113.
45. Poston, R.N., Haskard, D.O., Coucher, J.R., Gall, N.P., and Johnson-Tidey, R.R. 1992. Expression of intercellular adhesion molecule-1 in atherosclerotic plaques. *Am. J. Pathol.* 140:665–673.
46. Morisaki, N., et al. 1997. New indices of ischemic heart disease and aging: studies on the serum levels of soluble intercellular adhesion molecule-1 (ICAM-1) and soluble vascular cell adhesion molecule-1 (VCAM-1) in patients with hypercholesterolemia and ischemic heart disease. *Atherosclerosis.* 131:43–48.
47. Collins, R.G., et al. 2000. P-Selectin or intercellular adhesion molecule (ICAM)-1 deficiency substantially protects against atherosclerosis in apolipoprotein E-deficient mice. *J. Exp. Med.* 191:189–194.
48. Springer, T.A. 1990. Adhesion receptors of the immune system. *Nature.* 346:425–434.
49. Della Bella, S., et al. 2001. Novel mode of action of iloprost: in vitro down-regulation of endothelial cell adhesion molecules. *Prostaglandins Other Lipid Mediat.* 65:73–83.
50. Ishizuka, T., et al. 1998. Stimulation with thromboxane A_2 (TXA_2) receptor agonist enhances ICAM-1, VCAM-1 or ELAM-1 expression by human vascular endothelial cells. *Clin. Exp. Immunol.* 112:464–470.
51. Mitsuhashi, M., et al. 2001. Necessity of thromboxane A_2 for initiation of platelet-mediated contact sensitivity: dual activation of platelets and vascular endothelial cells. *J. Immunol.* 166:617–623.
52. Muller, W.A., Weigl, S.A., Deng, X., and Phillips, D.M. 1993. PECAM-1 is required for transendothelial migration of leukocytes. *J. Exp. Med.* 178:449–460.
53. Duncan, G.S., et al. 1999. Genetic evidence for functional redundancy of platelet/endothelial cell adhesion molecule-1 (PECAM-1): CD31-deficient mice reveal PECAM-1 dependent and PECAM-1-independent functions. *J. Immunol.* 162:3022–3030.
54. Graesser, D., et al. 2002. Altered vascular permeability and early onset of experimental autoimmune encephalomyelitis in PECAM-1-deficient mice. *J. Clin. Invest.* 109:383–392. doi:10.1172/JCI200213595.
55. Ensminger, S.M., et al. 2002. Platelet-endothelial cell adhesion molecule-1 (CD31) expression on donor endothelial cells attenuates the development of transplant arteriosclerosis. *Transplantation.* 74:1267–1273.
56. Newman, P.J. 1999. Switched at birth: a new family for PECAM-1. *J. Clin. Invest.* 103:5–9.
57. Rival, Y., Del Maschio, A., Rabiet, M.J., Dejana, E., and Duperray, A. 1996. Inhibition of platelet endothelial cell adhesion molecule-1 synthesis and leukocyte transmigration in endothelial cells by the combined action of TNF-α and IFN-γ. *J. Immunol.* 157:1233–1241.
58. Ma, H., et al. 2001. Increased bleeding tendency and decreased susceptibility to thromboembolism in mice lacking the prostaglandin E receptor subtype EP3. *Circulation.* 104:1176–1180.
59. Palinski, W., et al. 1994. ApoB-deficient mice are a model of lipoprotein oxidation in atherogenesis. Demonstration of oxidation-specific epitopes in lesions and high titers of autoantibodies to malondialdehyde-lysine in serum. *Arterioscler. Thromb.* 14:605–616.
60. Tangirala, R.K., Rubin, E.M., and Palinski, W. 1995. Quantitation of atherosclerosis in murine models: correlation between lesions in the aortic origin and in the entire aorta, and differences in the extent of lesions between sexes in LDL receptor-deficient and apolipoprotein B-deficient mice. *J. Lipid Res.* 36:2320–2328.
61. Sano, H., et al. 2001. Functional blockade of platelet-derived growth factor receptor-β but not of receptor-α prevents vascular smooth muscle cell accumulation in fibrous cap lesions in apolipoprotein E-deficient mice. *Circulation.* 103:2955–2960.
62. Murayama, T., et al. 2000. Over expression of low density lipoprotein receptor eliminates apolipoprotein B100-containing lipoproteins from circulation and markedly prevents early atherogenesis in apolipoprotein B-deficient mice. *Atherosclerosis.* 153:295–302.
63. Nakashima, Y., Raines, E.W., Plump, A.S., Breslow, J.L., and Ross, R. 1998. Upregulation of VCAM-1 and ICAM-1 at atherosclerosis-prone sites on the endothelium in the ApoE-deficient mouse. *Arterioscler. Thromb. Vasc. Biol.* 18:842–851.
64. Huo, Y., et al. 2003. Circulating activated platelets exacerbate atherosclerosis in mice deficient in apolipoprotein E. *Nat. Med.* 9:61–67.
65. Furchgott, R.P., and Zawadzki, J.V. 1980. The obligatory role of endothelial cells in the relaxation of arterial smooth muscle by acetylcholine. *Nature.* 288:373–376.
66. Poole, J.C.F., Sanders, A.G., and Florey, H.W. 1958. The regeneration of aortic endothelium. *J. Pathol. Bacteriol.* 75:133–143.
67. Massberg, S., et al. 2003. A crucial role of glycoprotein VI for platelet recruitment to the injured arterial wall in vivo. *J. Exp. Med.* 197:41–49
68. Furman, M.I., et al. 1998. Increased platelet reactivity and circulating monocyte-platelet aggregates in patients with stable coronary artery disease. *J. Am. Coll. Cardiol.* 31:352–358.
69. Michelson, A.D., and Furman, M.I. 1999. Laboratory markers of platelet activation and their clinical significance. *Curr. Opin. Hematol.* 6:342–348.

Role of Bone Marrow–Derived Progenitor Cells in Cuff-Induced Vascular Injury in Mice

Yang Xu, Hidenori Arai, Xin Zhuge, Hideto Sano, Toshinori Murayama, Momoko Yoshimoto, Toshio Heike, Tatsutoshi Nakahata, Shin-ichi Nishikawa, Toru Kita, Masayuki Yokode

Objectives—Arterial injury results in vascular remodeling associated with proliferation and migration of smooth muscle cells (SMCs) and the development of intimal hyperplasia, which is a critical component of restenosis after angioplasty of human coronary arteries and an important feature of atherosclerotic lesions. However, the origin of SMCs and other cells in the development of vascular remodeling is not yet fully understood.

Methods and Results—We utilized a cuff-induced vascular injury model after transplantation of the bone marrow (BM) from green fluorescent protein (GFP)-transgenic mice. We found that macrophages were major cells recruited to the adventitia of the vascular injury lesion along with SMCs and endothelial cells (ECs). While investigating whether those cells are derived from the donor, we found that most of the macrophages were GFP-positive, and some of the SMCs and ECs were also GFP-positive. Administration of the anti–c-*fms* antibody resulted in a marked decrease in macrophages and a relative increase of SMCs, while administration of antibodies against the platelet-derived growth factor receptor-β caused a prominent decrease in SMCs and a relative increase in macrophages.

Conclusions—The current study indicates that BM-derived cells play an important role in vascular injury, and that differentiation of macrophages and SMCs might be dependent on each other. (*Arterioscler Thromb Vasc Biol.* 2004; 24:477-482.)

Key Words: macrophage ■ smooth muscle cell ■ endothelial cell ■ vascular injury ■ bone marrow

Arterial injury results in proliferation and migration of smooth muscle cells (SMCs) and the development of intimal hyperplasia, a critical component of restenosis after angioplasty of human coronary arteries and an important feature of atherosclerotic lesions. However, the origin of SMCs, which engage in the development of neointimal thickening during vascular disease, is not yet fully understood. One possibility is that medial SMCs are phenotypically modified and migrate into the intima, where they proliferate and secrete extracellular matrix components.[1] It has also been proposed that adventitial fibroblasts move into the neointima and give rise to cells with smooth-muscle–like properties.[2]

Recently, several groups have reported that cells of recipient origin take part in the formation of neointimal SMCs during the development of transplant vasculopathy.[3–5] These results agree with the notion that adult bone marrow (BM) contains multipotent cells that can develop into various lineages.[6] It has also been shown that endothelial progenitor cells (EPCs) can transdifferentiate into SMCs.[7] Thus, the origin of SMCs in atherosclerotic lesions is a source of controversy, and it is important to understand the contribution of BM-derived cells to neointimal formation in vascular pathology.

In vascular injury or remodeling, it is not clear whether one specific type of multipotent precursor cell can differentiate into endothelial cells (ECs), SMCs, or macrophages, or whether there are different precursor cells for each cell lineage. We have reported that administration of anti–c-*fms* antibody can prevent early atherosclerosis in apolipoprotein E-deficient (apoE$^{-/-}$) mice.[8] We have also shown that administration of antibodies against the platelet-derived growth factor receptor-β (anti–PDGFR-β) can prevent the recruitment of SMCs, but not of macrophages in the atherosclerotic lesions in apoE$^{-/-}$ mice.[9] These results indicate the important role of macrophages in the initiation of the lesion and recruitment of SMCs in hyperlipidemia-induced atherosclerosis. However, it is not known whether the recruitment of macrophages is critical for the migration of SMCs in vascular injury.

Therefore, we have two goals in this study. One is to explore the contribution of BM-derived cells to the development of vascular remodeling. The other is to examine whether blocking the cell differentiation by a specific antibody can affect the lesion formation in vascular injury. For this purpose we have utilized an inflammation-dependent vascular disease

Received November 16, 2003; revision accepted January 5, 2004.

From the Departments of Geriatric Medicine (H.S.), Pediatrics (M. Yoshimoto, T.H., T.N.), and Cardiovascular Medicine (T.K.), Kyoto University Graduate School of Medicine, Japan; the Translational Research Center (Y.X., X.Z., T.M., M. Yokode), Kyoto University Hospital, Kyoto, Japan; and the RIKEN Center for Developmental Biology (S.N.), Kobe, Japan

Correspondence to Hidenori Arai, MD, PhD, Department of Geriatric Medicine, Kyoto University Graduate School of Medicine, 54 Kawahara-cho, Shogoin, Sakyo-ku, Kyoto, 606-8507, Japan. E-mail harai@kuhp.kyoto-u.ac.jp

Arterioscler Thromb Vasc Biol. is available at http://www.atvbaha.org

DOI: 10.1161/01.ATV.0000118016.94368.35

model induced by polyethylene cuff placement around the femoral artery after BM transplantation (BMT) from green fluorescent protein (GFP)-transgenic mice.

Methods

Mice

All experimental protocols were performed in accordance with the guidelines of Kyoto University, Japan. GFP-transgenic mice with C57BL/6 background were a generous gift from Dr. M. Okabe[10] (Osaka University, Japan). The mice were kept in a temperature-controlled facility on a 14-hour light/10-hour dark cycle, with free access to food and water. Mice were fed a normal chow diet containing 8.7% (wt/wt) fat and 0.063% (wt/wt) cholesterol (Oriental Yeast, Chiba, Japan) for the entire period of the experiment.

Bone Marrow Transplantation

Femurs of male or female, 8- to 12-week-old GFP-transgenic mice were dissected, and surrounding muscle tissue was removed by microscissors. Bones were then left in Dulbecco's modified Eagle's medium (DMEM). Both ends of the bones were cut with scissors, and the marrow was flushed with DMEM using a syringe with a 21-gauge needle. The marrow clusters were disaggregated by vigorous pipetting. BM cells were washed, resuspended in PBS, and counted. Eight-week-old female C57BL/6 mice were subjected to a lethal dose of total body irradiation (9 Gy) using the Gammacell 40 Exactor Irradiator (Nordion International). Each irradiated recipient received 5×10^5 BM cells extracted from GFP-transgenic mice in 0.5 mL PBS by tail vein injection. Mice used for BMT experiments were housed in sterilized cages and fed sterilized normal chow diet. Drinking water was supplied with 0.1% hydrochloric acid. Four weeks after BMT, the recipient mice were phlebotomized, and the circulating leukocytes were then checked for the expression of GFP by flow cytometry. Cuff placement was performed at least 4 weeks after BMT.

Cuff Placement

Mice were anesthetized with barbiturate complex [propylene glycol 17.9% (v/v), ethanol 8.9% (v/v), sodium 5-ethyl-5-(1-methylbutyl) barbiturate 10.7% (v/v)]. The right femoral artery was dissected from its surroundings. A nonconstrictive polyethylene cuff (PE50, 0.58 mm inner diameter, 0.965 mm outer diameter, 2 mm length; Becton Dickinson) was placed loosely around the right femoral artery.

Antibody Administration

AFS98, a rat monoclonal anti-murine c-*fms* antibody, which inhibits colony formation dependent on macrophage-colony stimulating factor (M-CSF) and cell growth by blocking the binding of M-CSF to its receptor c-*fms*, was previously described as an anti–c-*fms* antibody.[9] APB5, a rat monoclonal anti-murine PDGFR-β antibody, which blocks the PDGFR-β–mediated signaling pathway, was also described.[9] Four C57BL/6 mice in each group were administered 1 mg of AFS98, APB5, or isotype-matched irrelevant rat IgG (γ2A) once a day for 2 weeks after cuff placement.

Tissue Preparation

At euthanization, mice were anesthetized with barbiturate complex. Mouse thorax was opened, and physiological pressure-perfusion-fixation (100 mm Hg) was performed by cardiac puncture with 4% paraformaldehyde in PBS for 10 minutes. After the procedures, bilateral femoral arteries were harvested. The tissue was snap-frozen in OCT compound (Sakura Finetek). Serial cross sections (6 μm thick) were obtained throughout the entire length of the cuffed femoral artery or equivalent portion of the contralateral artery for histological analysis. Rat monoclonal antibody (mAb) BM8, labeled with biotin (BMA Biochemicals AG), was used as a specific marker for mouse macrophages. For macrophage staining, we used the Tyramide Signal Amplification system (NEN Life Science Products) to amplify the weak signal. For SMC staining, we used mouse monoclonal anti-human smooth muscle α-actin (SMA) antibody (clone 1A4), labeled with Cy3 (Sigma). For the staining of smooth muscle myosin heavy chain SM1,[11] we used rat anti-SM1 mAb (clone KM995) (kindly provided by the Kyowa Hakko Kogyo Co, Tokyo, Japan). Sections were secondarily incubated with rhodamine-labeled anti-rat IgG (Chemicon). ECs were identified by immunohistochemical staining with biotin-conjugated rat anti-mouse CD31 antibody (Southern Biotech) and rabbit anti–von Willebrand Factor (vWF) antibody (Sigma). For CD31 staining, the Tyramide Signal Amplification system was employed to augment antigenicity of ECs. For vWF staining, sections were secondarily incubated with rhodamine-labeled anti-rabbit IgG (Chemicon).

Image Analysis and Quantification

Eight equally crossed sections were used from each mouse to quantify the femoral artery lumen, BM-derived cell area, and vascular remodeling lesion size. Sections were evaluated by using Image-Pro Plus (Media Cybernetics). To estimate the effect of anti–c-*fms* or anti–PDGFR-β on vascular remodeling, we calculated the ratio of the number of SMCs or macrophages to the whole vascular remodeling lesion area. The area of the femoral artery lumen, BM-derived cells, and vascular remodeling lesion was calculated and expressed in square micrometers.

Statistical Analysis

Data are expressed as mean±SEM and were analyzed by ANOVA with Abacus Statview software (version 5.0). A value of $P<0.05$ was regarded as significant.

Results

Recruitment of Bone Marrow–Derived Progenitor Cells in Cuff-Induced Vascular Remodeling

To elucidate the involvement of BM-derived cells in cuff-induced vascular remodeling lesions, BM cells from GFP-transgenic mice were transplanted into lethally irradiated C57BL/6 mice before cuff placement. After 4 weeks of BMT, we confirmed the reconstitution of the hematopoietic system by checking the fluorescence of blood leukocytes by flow cytometry. We found that more than 85% of the cells were positive for GFP (data not shown); this finding indicates that most of the leukocytes were derived from the donor BM. One or two weeks after cuff placement, cuffed or sham-operated femoral arteries were examined under fluorescence microscopy. In the cuffed artery, the majority of the cells accumulating in the lesion were GFP-positive (Figure 1A and 1B), suggesting that those cells were derived from the donor BM. In contrast, in the sham-operated artery, GFP-positive cells were hardly detected (Figure 1C). We found that the accumulation of BM-derived cells in the vascular remodeling lesion was significantly increased from 1 week to 2 weeks after cuff placement (Figure 1A, 1B, and 1D). Although we did not find a visible change in intimal thickening after cuff placement, the lumen of the cuffed artery was more restricted than that of the sham-operated artery (Figure 1E).

Macrophages are the Major Component in the Cuff-Induced Vascular Remodeling Lesion

Next, to examine the recruitment of macrophages in the cuffed lesion, we stained the tissue with BM8. We found many cells recruited to the adventitia of the cuffed artery, most of which were positive for BM8 (Figure 2A), indicating the role of monocyte-macrophages in vascular remodeling

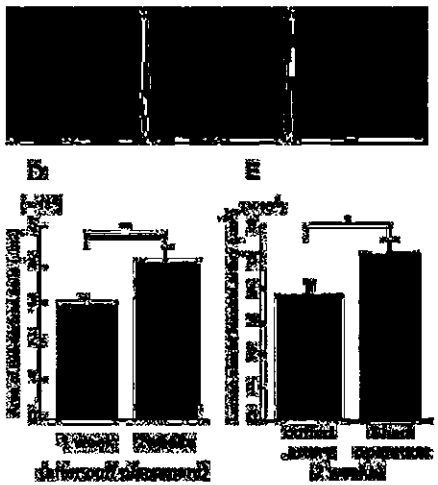

Figure 1. A through C, Representative microscopic photographs of BM-derived GFP-positive cells in C57BL/6 mouse vascular remodeling lesion. Four weeks after BMT, a nonconstrictive polyethylene cuff was placed around the right femoral artery in four mice in each group. The cuffed (A, 1 week after cuff placement; B, 2 weeks after cuff placement) or sham-operated (C) femoral arteries were examined under fluorescence microscopy. D and E, Quantitative analyses of BM-derived cell area (D) and femoral artery lumen area (E) after cuff placement showed a significant difference between 2 groups. Data from 20 slices per mouse artery are shown as mean±SEM. *$P<0.05$, **$P<0.01$. Scale bars: 100 μm

lesions. In the sham-operated femoral artery, we found few BM8-positive cells (Figure 2B).

BM Cells Can Differentiate into Vascular Smooth Muscle Cells

To examine whether BM-derived cells can differentiate into SMCs in the vascular remodeling lesion, we stained the tissue with Cy3-labeled anti-SMA (clone 1A4) and anti-SM1 (clone

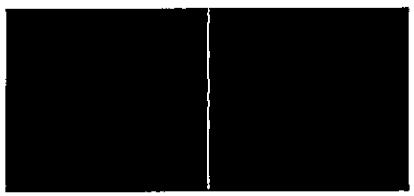

Figure 2. Numerous macrophage-like cells accumulating in the cuff-induced vascular remodeling lesion. After 2 weeks of cuff placement as described in Figure 1, tissues were subjected to immunohistochemistry with biotinylated anti-mouse macrophage antibody BM8. A number of cells were BM8-positive cells in cuffed femoral artery (A), but in the sham operated femoral artery, those cells could hardly be found (B). Scale bars: 100 μm

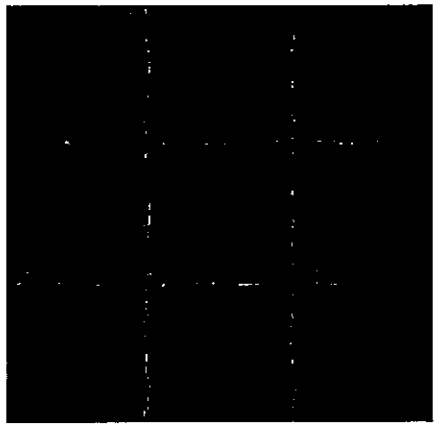

Figure 3. BM-derived SMCs in C57BL/6 mouse vascular remodeling lesion. After the same procedure in Figure 1, tissues were subjected to immunohistochemistry with antibodies to Cy3-labeled SMA (B, H) or SM1 (E). A, D, and G are fluorescent microscopic photographs for GFP. G, H, and I are fluorescent microscopic photographs from femoral artery of 1 week after cuff placement. All the others are samples at 2 weeks after cuff placement. C, F, and I are merged images of GFP and Cy3 signal from A and B, D and E, and G and H, respectively. Scale bars: 100 μm

KM995) antibodies. We found a number of 1A4- and KM995-positive cells in the adventitia of the lesion (Figure 3B and 3E). With the colorization of GFP signals, we observed that some of the 1A4- and KM995-positive cells were also positive for GFP (Figure 3C and 3F), indicating that BM-derived cells can also differentiate to SMCs in the cuff-induced vascular remodeling lesion. However, in the earlier time point at 1 week after cuff placement, we could find few SMCs in vascular remodeling lesion (Figure 3H).

Interference Exists Between Macrophages and Smooth Muscle Cells

To examine whether inhibiting the differentiation to macrophage or SMC by mAb could affect the manner of accumulation and differentiation of BM-derived cells in the vascular remodeling lesion, we administered an antagonistic rat mAb against murine *c-fms* (M-CSF receptor) (clone AFS98) or PDGFR-β (clone APB5) to C57BL/6 female mice which had undergone cuff placement. In comparison with the lesion from mice administered with control IgG (clone γ2A) (Figure 4C), we found that the treatment with AFS98 caused a marked decrease in macrophages in the lesion (Figure 4A and 4G). Interestingly, the density of SMCs was inversely increased (Figure 4D and 4H) in response to this treatment. In contrast, administration of APB5 resulted in a marked increase in macrophages (Figure 4B and 4G) with a concomitant decrease of SMCs (Figure 4E and 4H), suggesting that a certain interaction occurs between macrophages and SMCs during the vascular remodeling process.

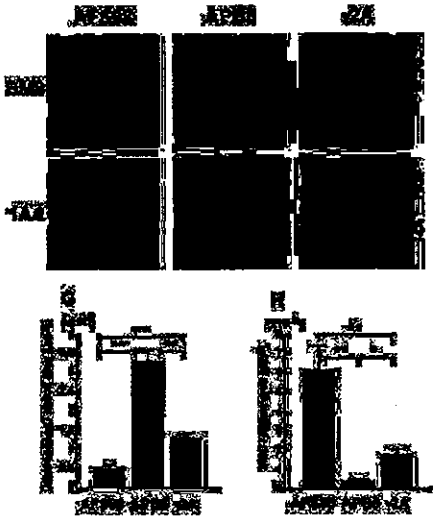

Figure 4. Progenitors of SMC and macrophage have opposite roles in the lesion formation. A total of 12 C57BL/6 mice (8 weeks of age) were injected for 2 weeks with 1 mg of AFS98 (n=4), APB5 (n=4), or γ2A (n=4) every day after cuff placement. Each mouse was euthanized and the femoral artery was subjected to immunohistochemistry with anti-macrophage antibody (A, B, and C) or anti-SMA antibody (D, E, and F). A and D are from mice injected with AFS98, B and E are from mice injected with APB5, and C and F are from mice given γ2A. Ratio of the number of macrophages (G) and SMCs (H) to whole vascular remodeling lesion area had a significant difference in each group. Data from 20 slices per mouse are shown as mean±SEM. *$P<0.05$, **$P<0.01$. Scale bars: 100 μm

To estimate the effects of anti–PDGFR-β or anti–*c-fms* mAb on vascular remodeling, we measured the lumen size of the artery treated with the two kinds of mAb and γ2A. We found no distinct difference in the lumen size of the femoral artery through administration of AFS98, APB5, or γ2A (data not shown).

We also examined whether each antibody administration had any effect on tissue formation after cuff placement. The calculated vascular remodeling lesion area of each mouse treated with AFS98, APB5, and γ2A was $1.18\times10^5\pm5.38\times10^3$ μm², $1.43\times10^5\pm7.27\times10^3$ μm², and $1.82\times10^5\pm1.11\times10^4$ μm², respectively (mean±SEM of 20 slices from each of 4 mice, $P<0.05$ versus γ2A). Less tissue formation was observed in the mice treated with AFS98 and APB5 than in mice treated with γ2A. This result indicates that AFS98 and APB5 administration could inhibit tissue formation after cuff placement. Further, to examine whether APB5 or AFS98 has an effect on BM-derived cell incorporation, we performed cuff placement and administered each antibody to mice that had been subjected to BMT. By measuring BM-derived cells accumulating in the cuff-induced lesion, we found a significant decrease of GFP-positive cells by mAb administration (data not shown), indicating that APB5 and AFS98 also affected the incorporation of BM-derived cells.

Figure 5. Representative microscopic photographs of BM-derived ECs in cuff-induced vascular remodeling lesion. After the same procedure in Figure 1, tissues were subjected to immunohistochemistry with biotin-conjugated rat anti-mouse CD31. The microscopic photograph of A is from cuffed right femoral artery, and B is from sham-operated left femoral artery. Scale bars: 100 μm

Endothelial Progenitor Cells Are Recruited to the Cuffed Vascular Remodeling Lesion

Because it is not known whether EPCs can contribute to cuff-induced vascular remodeling lesion formation in the injured femoral artery, we performed a series of endothelial staining. We found that the endothelial lining of the intima was clearly stained with anti-CD31 antibody, and that small vessels in the adventitia were also stained. There were also some CD31-positive cells clustered outside the small vessels in the adventitia in the cuffed lesions (Figure 5A), but not in the sham-operated lesions (Figure 5B). Because CD31 can also be expressed on monocyte-macrophages, we stained the tissue with anti-vWF antibody, another EC-specific marker, and compared the expression with GFP-positive cells. As shown in Figure 6E, the endothelial lining of the intima and small vessels in the adventitia were also positive for vWF. Some of the clustered cells in the adventitia were positive for

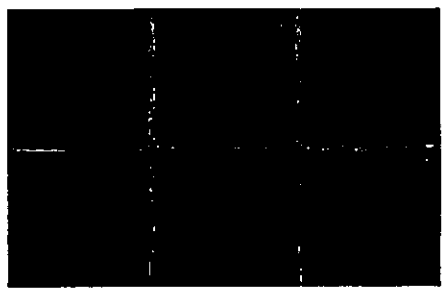

Figure 6. EPCs in cuff-induced vascular remodeling lesions. After the same procedure in Figure 1, tissues were subjected to immunostaining with anti-vWF antibody. A, B, and C are 1 week after cuff placement, and D, E, and F are 2 weeks after cuff placement. A and D indicate GFP signals, and B and E indicate vWF signals. C is a merged image of A and B, and F is a merged image of D and E. Scale bars: 100 μm

vWF and GFP, while the endothelial lining of the intima of the artery and small vessels in the adventitia were only positive for vWF (Figure 6F), indicating the involvement of angiogenesis from vasa vasorum. Notably, as we observed that significantly fewer SMCs could be found 1 week after cuffing (Figure 3B), EPCs could scarcely be found in the vascular remodeling lesion at this earlier phase (Figure 6C).

Discussion

In this study, we have clearly shown that BM-derived cells are critically involved in the lesion formation of cuff-induced vascular remodeling in mice. In this setting, BM-derived macrophages, SMCs, and ECs contributed to the lesion formation. However, not all of the SMCs or ECs in the lesion were derived from the BM. Interestingly, when anti–c-*fms* antibody was administered after cuff placement, the recruitment of macrophages was suppressed, but the density of SMCs was increased. On the other hand, administration of anti–PDGFR-β inhibited the recruitment of SMCs in the vascular remodeling lesion, but increased the number of macrophages. These results suggest an interaction between macrophages and SMCs during the lesion formation.

Although previous investigators have shown intimal thickening in the cuff-induced vascular injury model,[12,13] we have not been able to reproduce their results. This may be due to the technique of the cuff placement, because we were able to induce intimal thickening of the cuffed artery when we used apoE$^{-/-}$ mice fed with high-fat diet (data not shown). Indeed, we found a marked inflammatory change in the adventitial region around the cuffed artery. However, little is known about inflammatory responses in the adventitia after vascular injury, and adventitial and perivascular reactions are largely ignored. Recent clinical and experimental data by other investigators suggest that constrictive vascular remodeling is in large part responsible for lumen loss associated with restenosis.[14,15] Scott et al have indicated that the adventitia may be important in the first wave of growth after angioplasty of coronary arteries, with later growth of the lesion occurring in the neointima.[16] Therefore, studying the mechanism of cell recruitment to the adventitia in the vascular remodeling region is important for the understanding of the pathogenesis of restenosis.

Recent studies for transplant atherosclerosis have demonstrated that most of the neointimal α-actin–positive SMCs in recipient coronary arteries or aortas were from host origin,[4,5] suggesting that these SMCs might be at least in part from BM-derived smooth muscle progenitor cells. In this study, we have demonstrated that at least three types of cells, macrophage, SMC, and EC, are recruited from the BM to the adventitia of the cuff-induced vascular injury site. The characteristic feature of those cells is to form a cluster in the lesion. However, we have not determined when and how those cells migrate to the adventitia. Therefore, it is very important to understand the timing and pathway of cell migration in the pathogenesis of vascular injury. Elucidating the involvement of soluble factors in this model, such as chemokines and adhesion molecules, would also be intriguing.

In this study we have shown that administration of anti–c-*fms* antibody inhibited the recruitment of macrophages, and increased the recruitment of SMCs to the vascular injury lesion in wild-type mice. This finding is different from our report on apoE$^{-/-}$ mice, where we showed that the antibody inhibited the recruitment of SMCs as well as macrophages in early atherosclerotic lesion.[8] Thus, in hyperlipidemia-induced atherosclerosis, the recruitment of monocyte-macrophage is prerequisite for the migration of SMCs for the lesion formation; this paradigm was not applied to the current vascular injury model. If the common progenitors for macrophage and SMC exist, our data might indicate that BM-derived cells are playing an important role in vascular injury, but not in hyperlipidemia-induced atherosclerosis. The result with anti–PDGFR-β is also different from our previous observation in apoE$^{-/-}$ mice,[9] in which the antibody to apoE$^{-/-}$ mice failed to affect the density of macrophages in advanced atheromatous lesions. It was also notable that administration of anti–PDGFR-β increased the recruitment of macrophages in this study. Thus, in the vascular injury model, blocking the differentiation of one cell type can increase the recruitment or differentiation of the other cell type. Although we have not determined whether the progenitors of macrophages and SMCs are derived from the same precursor cell, anti–c-*fms* or anti–PDGFR-β might affect the differentiation of common precursor cells.

Schmeisser et al reported that BM-derived macrophages might contribute to neovascularization by in situ transdifferentiation to EC-like cells.[17] We found that in the vascular injury lesion there were many cells positive for CD31, which is an endothelial marker and is also positive for monocyte-lineage. However, vWF-positive cells were much smaller in number in this lesion. Furthermore, most of the cells forming a small vessel were positive for vWF, but negative for GFP, indicating that the source of the ECs forming a small vessel in the adventitia is from vasa vasorum, not from the BM.

Terada et al[18] and Ying et al[19] demonstrated that embryonic stem cells can spontaneously fuse with mononuclear BM cells[18] or brain cells[19] in vitro to form pluripotent tetraploid hybrids. In this study, there are a number of BM-derived cells stimulated after cuff placement in the cuff-induced vascular remodeling lesion. These BM-derived cells play an important role for lesion formation. Those two reports showed that the frequency of cell fusion was very low (2×10^{-6} to 10^{-4}), although it is difficult to directly correlate the in vitro findings of embryonic stem cells to our in vivo study. It is possible that some of the BM-derived cells in our experiments resulted from fusion between BM cells and vascular cells; however, this phenomenon would be an unlikely explanation for the extent of BM involvement seen in this study.

In summary, we have provided evidence that BM-derived cells are playing a critical role in cuff-induced vascular injury in mice. Understanding the interaction among the cells involved in the lesion formation will be important for regulating the accumulation of inflammatory cells in the vascular injury lesion.

Acknowledgments

This study was supported by Grants-in-Aid from the Ministry of Education, Science, Sports, and Culture of Japan (20045982, 12671111, 14571093, and 13307034) (to H.A., M.Y., T.K.); Center of Excellence grants (12CE2006) (to T.K.); a research grant for health sciences from the Japanese Ministry of Health and Welfare (to T.K.); and a grant from the Rotary Yoneyama Memorial Foundation (to Y.X.). T.M. is supported by Establishment of International COE for Integration of Transplantation Therapy and Regenerative Medicine (COE Program of the Ministry of Education, Culture, Sports, Science, and Technology, Japan). We thank Drs Hiroharu Kataoka and Masafumi Morimoto for their advice about cuff placement, and Akiko Kato for her excellent technical assistance.

References

1. Newby AC, Zaltsman AB. Molecular mechanisms in intimal hyperplasia. *J Pathol.* 2000;190:300–309.
2. Zalewski A, Shi Y. Vascular myofibroblasts. Lessons from coronary repair and remodeling. *Arterioscler Thromb Vasc Biol.* 1997;17:417–422.
3. Plissonnier D, Nochy D, Poncet P, Mandet C, Hinglais N, Bariety J, Michel JB. Sequential immunological targeting of chronic experimental arterial allograft. *Transplantation.* 1995;60:414–424.
4. Hillebrands JL, Klatter FA, van den Hurk BM, Popa ER, Nieuwenhuis P, Rozing J. Origin of neointimal endothelium and α-actin–positive smooth muscle cells in transplant arteriosclerosis. *J Clin Invest.* 2001;107:1411–1422.
5. Saiura A, Sata M, Hirata Y, Nagai R, Makuuchi M. Circulating smooth muscle progenitor cells contribute to atherosclerosis. *Nat Med.* 2001;7:382–383.
6. Pittenger MF, Mackay AM, Beck SC, Jaiswal RK, Douglas R, Mosca JD, Moorman MA, Simonetti DW, Craig S, Marshak DR. Multilineage potential of adult human mesenchymal stem cells. *Science.* 1999;284:143–147.
7. DeRuiter MC, Poelmann RE, VanMunsteren JC, Mironov V, Markwald RR, Gittenberger-de Groot AC. Embryonic endothelial cells transdifferentiate into mesenchymal cells expressing smooth muscle actins in vivo and in vitro. *Circ Res.* 1997;80:444–451.
8. Murayama T, Yokode M, Kataoka H, Imahayashi T, Yoshida H, Sano H, Nishikawa S, Kita T. Intraperitoneal administration of anti–c-*fms* monoclonal antibody prevents initial events of atherogenesis but does not reduce the size of advanced lesions in apolipoprotein E-deficient mice. *Circulation.* 1999;99:1740–1746.
9. Sano H, Sudo T, Yokode M, Murayama T, Kataoka H, Takakura N, Nishikawa S, Nishikawa SI, Kita T. Functional blockade of platelet-derived growth factor receptor-β but not of receptor-α prevents vascular smooth muscle cell accumulation in fibrous cap lesions in apolipoprotein E-deficient mice. *Circulation.* 2001;103:2955–2960.
10. Okabe M, Ikawa M, Kominami K, Nakanishi T, Nishimune Y. 'Green mice' as a source of ubiquitous green cells. *FEBS Lett.* 1997;407:313–319.
11. Nagai R, Kuro-o M, Babij P, Periasamy M. Identification of two types of smooth muscle myosin heavy chain isoforms by cDNA cloning and immunoblot analysis. *J Biol Chem.* 1989;264:9734–9737.
12. Liu HW, Iwai M, Takeda-Matsubara Y, Wu L, Li JM, Okumura M, Cui TX, Horiuchi M. Effect of estrogen and AT1 receptor blocker on neointima formation. *Hypertension.* 2002;40:451–457; discussion 448–450.
13. Suzuki J, Iwai M, Nakagami H, Wu L, Chen R, Sugaya T, Hamada M, Hiwada K, Horiuchi M. Role of angiotensin II-regulated apoptosis through distinct AT1 and AT2 receptors in neointimal formation. *Circulation.* 2002;106:847–853.
14. Mintz GS, Popma JJ, Pichard AD, Kent KM, Satler LF, Wong C, Hong MK, Kovach JA, Leon MB. Arterial remodeling after coronary angioplasty: a serial intravascular ultrasound study. *Circulation.* 1996;94:35–43.
15. Sangiorgi G, Taylor AJ, Farb A, Carter AJ, Edwards WD, Holmes DR, Schwartz RS, Virmani R. Histopathology of postpercutaneous transluminal coronary angioplasty remodeling in human coronary arteries. *Am Heart J.* 1999;138:681–687.
16. Scott NA, Cipolla GD, Ross CE, Dunn B, Martin FH, Simonet L, Wilcox JN. Identification of a potential role for the adventitia in vascular lesion formation after balloon overstretch injury of porcine coronary arteries. *Circulation.* 1996;93:2178–2187.
17. Schmeisser A, Garlichs CD, Zhang H, Eskafi S, Graffy C, Ludwig J, Strasser RH, Daniel WG. Monocytes coexpress endothelial and macrophagocytic lineage markers and form cord-like structures in Matrigel under angiogenic conditions. *Cardiovasc Res.* 2001;49:671–680.
18. Terada N, Hamazaki T, Oka M, Hoki M, Mastalerz DM, Nakano Y, Meyer EM, Morel L, Petersen BE, Scott EW. Bone marrow cells adopt the phenotype of other cells by spontaneous cell fusion. *Nature.* 2002;416:542–545.
19. Ying QL, Nichols J, Evans EP, Smith AG. Changing potency by spontaneous fusion. *Nature.* 2002;416:545–548.

Successful endovascular repair of an aneurysm of the ductus diverticulum with a branched stent graft: Case report and review of literature

Naritatsu Saito, MD,[a] Takeshi Kimura, MD,[a] Masanao Toma, MD,[a] Masakazu Teragaki, MD,[b] Hiroyoshi Minaminimura, MD,[c] Toru Kita, MD,[a] and Kanji Inoue, MD,[d] *Kyoto, Japan*

Aneurysm of the ductus diverticulum rarely has been reported in adults, and the reported aneurysms were treated with conventional open surgery or were diagnosed at autopsy. We report a successful endovascular repair of an aneurysm of the ductus diverticulum with the Inoue branched stent graft. In a 78-year-old woman, an abnormal shadow was noted at the aortopulmonary window on a chest x-ray film. A computed tomography scan demonstrated a 3.8-cm saccular aneurysm, which protruded inferiorly from the distal end of the aortic arch. The aneurysm was considered an aneurysm of the ductus diverticulum, and surgery was required. However, the patient was considered at high risk for respiratory dysfunction with conventional open surgery. Endovascular repair with an Inoue single-branched stent graft was performed with the patient under local anesthesia, successfully and without complication or endoleak. To our knowledge, this is the first report of endovascular treatment of an aneurysm of the ductus diverticulum. (J Vasc Surg 2004;40:1228-33.)

Aneurysm of the ductus diverticulum is rare in adults, and most reported cases were repaired with surgery.[1-11] Transluminal endovascular stent-graft placement in patients with thoracic aortic aneurysm is emerging as an attractive alternative to conventional open surgery.[12,13] However, its application is limited to descending thoracic aortic aneurysms distal to the aortic arch. Endovascular repair of aneurysms of the thoracic aortic arch is challenging. One option is to perform a surgical bypass from either the proximal ascending aorta or the femoral arteries[14,15]; another is to use a stent graft with side branches to the innominate, left carotid, and left subclavian arteries.[16-19] Except for the Inoue branched stent graft, reports of endovascular techniques of repair of complex aneurysms with branched stent grafts have been limited to animal studies and incidental case reports.[16-18] In March 2003 we began performing endovascular repair of aortic aneurysms in various locations with the Inoue stent graft, after approval of our ethics committee. We performed a successful endovascular repair of the aneurysm of the ductus diverticulum with a single-branched Inoue stent graft. To our knowledge, this is the first report of endovascular treatment of an aneurysm of the ductus diverticulum.

From the Department of Cardiovascular Medicine, Kyoto University,[a] the Department of Cardiology, Wakakusa Daiich Hospital,[b] the Department of Cardiovascular Surgery, Osaka General City Hospital,[c] and the Department of Cardiovascular Surgery, Takeda Hospital.[d]

Competition of interest: none.

Reprint requests: Naritatsu Saito, MD, Graduate School of Medicine, Kyoto University, Department of Cardiovascular Medicine, Sakyo Ku Shogoin Kawahara-tyo 54, Kyoto, Kyoto 606-8507, Japan (e-mail: naritatu@kuhp.kyoto-u.ac.jp

0741-5214/$30.00

doi:10.1016/j.jvs.2004.08.045

CASE REPORT

A chest roentgenogram in a 78-year-old woman indicated a subtle abnormal prominence. Computed tomography (CT) scans revealed a saccular aneurysm originating from the aortic arch in the aortopulmonary window. The aneurysm diameter was 3.8 cm (Fig 1, *A*). A 3-dimensional (3-D) CT scan showed that the aneurysm was located in a minor curvature of the distal aortic arch at the bifurcation of the left subclavian artery. The aneurysm end was in the direction of the top of the left pulmonary artery (Fig 1, *B*). On the basis of findings on the 3-D CT scan, a diagnosis of aneurysm of the ductus diverticulum was made. An aortogram demonstrated a saccular aneurysm at the distal aortic arch, and a coronary angiogram revealed no stenosis of the coronary arteries. The patient had a history of tuberculosis and chronic obstructive lung disease. Pulmonary function tests demonstrated severe pulmonary dysfunction: forced vital capacity, 1.45 L; forced expiratory volume in 1 second, 0.83 L; FVC-FEV_1 ratio, 57.0%. Thoracotomy was considered high risk, and the patient was referred to Kyoto University Hospital for endovascular stent grafting. After obtaining informed consent from the patient and approval from our institutional review board, we performed endovascular repair with a single-branched Inoue stent graft.

The endovascular Inoue stent-grafting system and its implantation techniques have been described in detail.[19-21] The Inoue stent graft was custom made for the patient, with a computer-assisted stent-graft design system.[22] A 3-D model was constructed from helical CT images of the aneurysm. The stent graft was designed and positioned endoluminally on the computer. The diameter of the aorta in the proximal position of the stent graft was 32 mm, 26 mm in the distal position of the stent graft, and 9 mm in the left subclavian artery. The diameter of the designed stent graft was 34 mm in the proximal neck, 28 mm in the distal neck, and 10 mm in the branch. The diameter of the aortic section of the graft was oversized by 2 mm, and by 1 mm in the branched section, to achieve effective sealing. The length of the graft at the center was 85 mm.

With the patient under local anesthesia, the right femoral artery was surgically isolated and a transverse arteriotomy was performed. A 7F sheath was inserted percutaneously in the left brachial artery. A 22F introducer sheath was inserted through the right femoral artery, and was advanced to the descending thoracic aorta under fluoroscopic guidance. After administration of 10,000 U of heparin, the folded branched stent graft was introduced into

Fig 1. a, Enhanced 2-dimensional computed tomography scan demonstrates 3 circles located in a hook shape beneath aortic arch (*arrows*), or the "triple star sign." Maximum diameter of the aneurysm is 3.8 cm. Atherosclerotic changes in adjacent aorta were not found. Diameter of descending aorta is 2.6 cm. **b**, Three-dimensional reconstructions of computed tomography scan show the aneurysm projecting to the left pulmonary artery from the minor curvature of the aortic arch. Aneurysm had thrombus, and compressed the left pulmonary artery.

Table 1. Confirmed cases of aneurysm of the ductus diverticulum reported in literature

Author (year)	*Language*	*Number of patients*	*Course*
Mitchell et al (1983)[1]	English	21	Six patients: underwent successful repair Another patients: died before or after surgery
Kitahara et al (1986)[2]	English	1	Successfully repaired
Tsujimoto et al (1987)[3]	English	1	Refused surgery, died of rupture
Baisden et al (1989)[4]	English	1	Successfully repaired
Ueno et al (1990)[5]	English	3	Successfully repaired in all patients
Baker et al (1993)[6]	English	1	Successfully repaired
Okada et al (1993)[23]	Japanese	1	Successfully repaired
Hattori et al (1994)[24]	Japanese	1	Successfully repaired
Shichijo (1994)[25]	Japanese	1	Successfully repaired
Taneja et al (1997)[7]	English	2	Successfully repaired in all patients
Ferrera et al (1997)[8]	English	1	Successfully repaired
Shimazaki et al (1998)[9]	English	1	Successfully repaired
Kido et al (1998)[10]	English	1	Successfully repaired
Jinnno et al (2002)[26]	Japanese	1	Successfully repaired
Sugimoto et al (2003)[11]	English	2	Successfully repaired in all patients

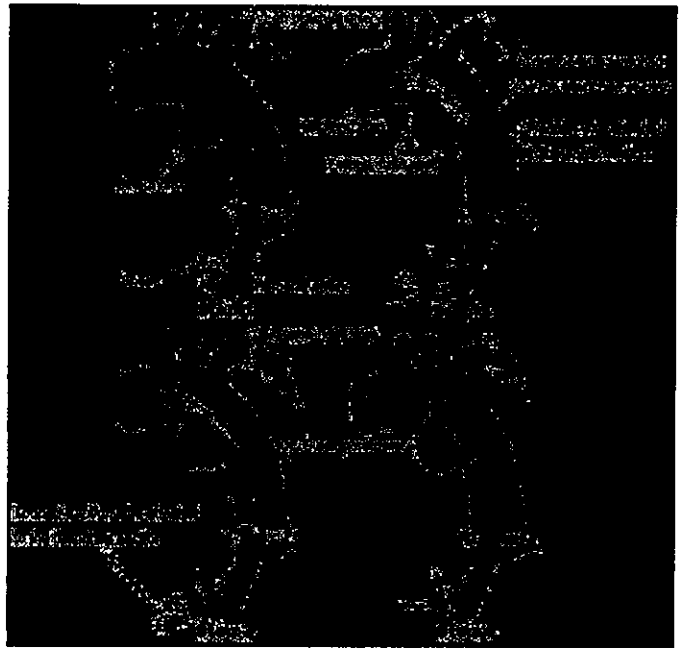

Fig 2. Technique of single-branched stent-graft placement. Step 1, 22F introducer sheath is inserted in the descending thoracic aorta through the right femoral artery. Step 2, Folded stent graft is advanced to the descending thoracic aorta with a carrying wire. Step 3, 10F guiding catheter is inserted through the introducer sheath, along with the traction wire attached to the branched section. Free end of traction wire is inserted in the 10F guiding catheter and caught by the gooseneck wire. Step 4, Stent graft is unfolded and dilated with balloon inflation. Finally, carrying wire and traction wire are detached.

the sheath, advanced to the ascending aorta, and released from the sheath. Then the folded graft was advanced to the distal aortic arch. A 7F catheter with gooseneck wire was inserted through the 7F sheath in the left brachial artery. The free end of the traction wire attached to the tip of the branched graft section was caught by the gooseneck wire and pulled back into the left subclavian artery. With manipulation of the carrying wire and traction wire, the aortic and branched graft sections were properly positioned. After unfolding the branched graft, the aortic section and the branched section of the graft were dilated with a compliant balloon. The balloon was custom-made, and inserted through the 22F sheath. We did not use hypotension to place the graft or for balloon inflation. Implantation technique is shown in Fig 2. Aortograms confirmed that the graft was placed at the proper position and that the aneurysm was completely excluded. Fig 3 depicts aortograms obtained before and after endovascular repair. Finally, all delivery systems were removed and the arteriotomy was closed. An intimal injury of the right external iliac artery occurred during introduction of the 22F sheath, which was repaired successfully with implantation of a Palmaz stent. No other complications occurred during the procedure. Total procedure time was 190 minutes, and volume of contrast media used was 143 mL. The postoperative course was uneventful. A CT scan obtained 10 days after the procedure demonstrated complete exclusion of the aneurysm, and no endoleak was detected (Fig 4). The patient was discharged 12 days after the stent grafting, without any disorders. She remained in the hospital for more than a week for social reasons, but could have been discharged as early as postoperative day 2.

DISCUSSION

Aneurysm of the ductus diverticulum is rarely reported in adults, and preoperative diagnosis is difficult.[1-6] With the advent of more sophisticated diagnostic methods, preoperative recognition of these aneurysms is more frequent. We found 39 reports of aneurysm of the ductus diverticulum in the literature (Table).[1-11,23-26] The aortic end of the ductus diverticulum is patent, whereas the pulmonary end is usually closed. The aneurysm forms as a result of incomplete closure of the ductus arteriosus in its aortic site, from pressure overload, such as hypertension and atherosclerotic changes of aging. The 3-D CT scan, in which 3 circles are located in a hook shape beneath the aortic arch, is called the "triple star sign," and this finding was reported to be a typical sign of this disease.[5] Sugimoto et al[11] reported that a 2D CT scan is useful for differentiation of aneurysm of the ductus diverticulum from common atherosclerotic aneurysm. Compared with atherosclerotic aneurysm in the distal aortic arch, aneurysm of the ductus diverticulum is located in the minor curvature of the distal aortic arch, at the bifurcation of the left subclavian artery, and the direction of the aneurysm end is toward the top of the left subclavian artery. The diagnosis of aneurysm of the ductus diverticulum was made with contrast-enhanced 2-D and 3-D CT scans in our patient.

There is little information about the size of aneurysms of the ductus diverticulum that ruptured. We found 39 cases in 15 reports. Only 2 articles reported patients who died before surgery. Tsujimoto et al[8] reported a patient who refused surgery, and that patient died of rupture of the aneurysm. The maximum diameter of the aneurysm was 11.8 cm. Mitchell et al[1] reported their experience with successful repair of 5 aneurysms of the ductus diverticulum. They reviewed the literature, and found 16 cases. Ten of these patients died of rupture of the aneurysm or a related complication before surgery. The minimum diameter of the ruptured aneurysm was 4 × 3 cm. They concluded that aneurysm of the ductus diverticulum is frequently fatal, even when small compared with saccular atherosclerotic aneurysms. They recommend surgical intervention for aneurysms of the ductus diverticulum greater than 3 cm in greatest diameter. However, this report was published 20 years ago. Most recent reports are case reports or case series of successful surgical repair.[2,4-11,23-26] Therefore the natural history of this rare aneurysm is still unknown. The aneurysm diameter was 3.8 cm in our patient, and thoracotomy was considered too high risk because of the patient's severe pulmonary dysfunction and advanced age. Transluminal endovascular stent grafting was considered suitable in this patient. Although the safety and efficacy of stent-graft placement in thoracic aortic aneurysms has been reported, placement of these stent grafts was limited to sites

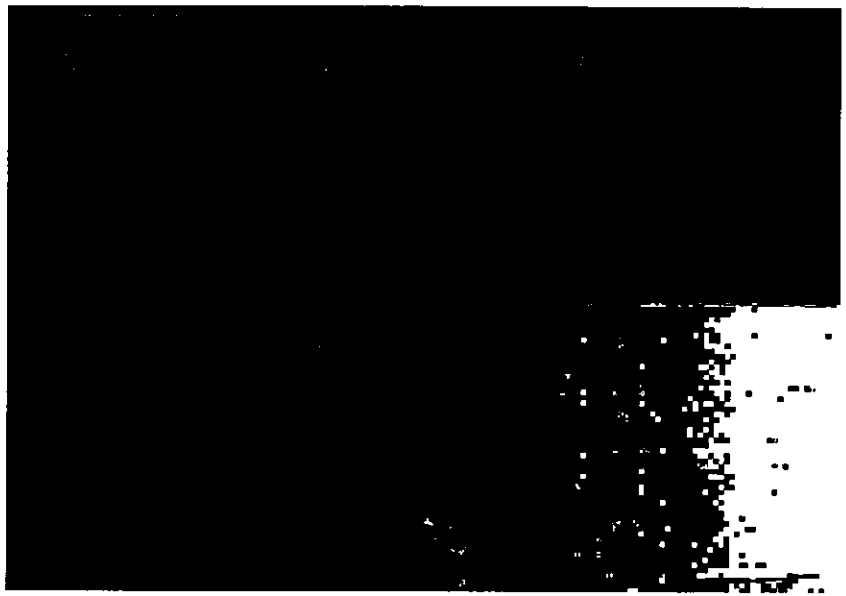

Fig 3. A, Preprocedural angiogram shows the aneurysm. B, Folded stent graft is advanced. C, Aortic section of graft is dilated. D, Branched section of graft is dilated. E, No endoleak is seen on final angiogram.

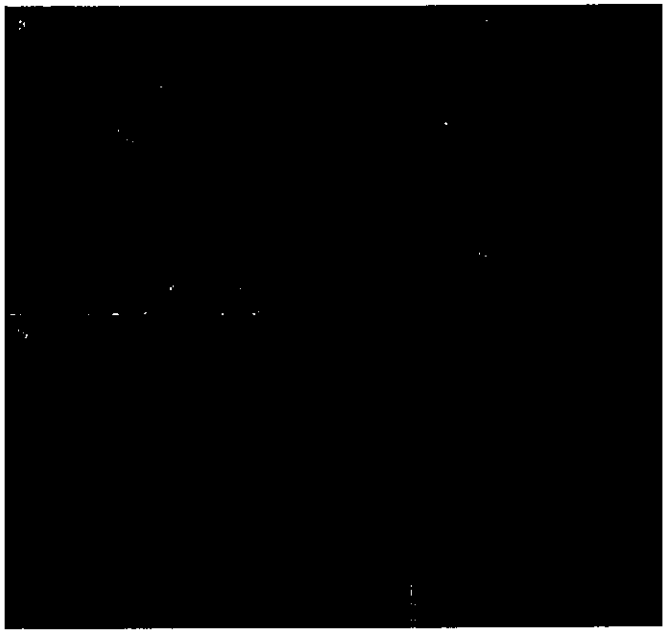

Fig 4. Two-dimensional *(top)* and 3-dimensional *(bottom)* computed tomography scans demonstrate complete exclusion of aneurysm.

that did not include the origin of the major aortic arterial branches.[12,13] Aneurysm of the ductus diverticulum is located at the aortic arch, and a single-branched stent graft was required. The major complication of the branched Inoue stent graft in thoracic aortic aneurysms is cerebral infarction.[19] Unlike true atherosclerotic aneurysms, there was little arteriosclerosis in the aortic wall in this patient, and the risk for cerebral infarction was estimated to be low. We estimated that the risk for rupture outweighed the risk of stent grafting in this patient.

Implantation of a single-branched Inoue stent graft to treat aneurysm of the ductus devirticulum was successful, without complications or endoleak. However, because the procedure was performed only 2 months before the writing of this report, only early success can be confirmed. Inasmuch as true success of endovascular stent-graft repair is determined with long-term results, careful long-term evaluation is needed.

REFERENCES

1. Mitchell RS, Seifert FC, Miller DC, Jamieson SW, Shumway NE. Aneurysm of the diverticulum of the ductus arteriosus in the adult. Successful surgical treatment in five patients and review of the literature. J Thorac Cardiovasc Surg 1983;86:400-8.
2. Kitahara Y, Kanazawa N, Sasaki T, Araki R, Kogure S, Tsuchiya Y, et al. Aneurysm of a diverticulum of the ductus arteriosus in an adult: a case report. J Cardiogr 1986; 16:259-67.
3. Tanjimoto S, Hirose K, Ohyagi A. A ruptured large aneurysm of the ductus arteriosus. Br Heart J 1987;57:289-91.
4. Baisden CE, Sand ME, Keith SC, Jackson JF, Mullen PE, Brown WH. Ductus diverticulum aneurysm and coronary stenosis: repair using circulatory arrest. Ann Thorac Surg 1989;48:432-3.
5. Ueno Y, Shinozaki T, Shimamoto M, Ohkubo K, Ueda M, Akiyama F. Aneurysm of the diverticulum of the ductus arteriosus in the adult. Nippon Kyobu Geka Gakkai Zasshi 1990;38:1356-61.
6. Baker J, Julsrud P, Welch T. Traumatic rupture of the aorta with ductus diverticulum: a case history. Angiology 1993;44:248-50.
7. Taneja K, Gulati M, Jain M, Saxena A, Das B, Rajani M. Ductus arteriosus aneurysm in the adult: role of computed tomography in diagnosis. Clin Radiol 1997;52:231-4.
8. Ferrera PC, Ghaemmaghami PA. Ductus diverticulum interpreted as traumatic aortic injury. Am J Emerg Med 1997;15:371-2.
9. Shimazaki Y, Inui K, Watanabe T, Minowa T, Kuraoka S, Oshikiri N, et al. Ruptured aneurysm of the ductus diverticulum into the pulmonary artery in a man: a successful repair. J Cardiovasc Surg (Torino) 1998; 13:146-9.
10. Kido M, Kawaguchi H, Ninomiya H, Osako M, Otani H, Imamura H. One stage operation for aneurysm of the diverticulum of the ductus arteriosus and coronary artery bypass grafting. Jpn J Thorac Cardiovasc Surg 1998;46:1024-7.
11. Sugimoto T, Takahashi T, Inui K, Minowa T, Watanabe T, Shimazaki Y. Aneurysm of the ductus diverticulum in adults: the diagnostic value of three dimensional computed tomographic scanning. Jpn J Thorac Cardiovasc Surg 2003;51:524-7.
12. Dake MD, Miller DC, Semba CP, Mitchell RS, Walker PJ, Liddell RP. Transluminal placement of endovascular stent-grafts for the treatment of descending thoracic aortic aneurysms. N Engl J Med 1994; 331:1729-34.
13. Bell RE, Taylor PR, Aukett M, Sabharwal T, Reidy JF. Mid-term results for second-generation thoracic stent grafts. Br J Surg 2003;90:811-7.
14. Criado FJ, Barnatan MF, Rizk Y, Clark NS, Wang CF. Technical strategies to expand stent-graft applicability in the aortic arch and proximal descending thoracic aorta. J Endovasc Ther 2002;9(Suppl 2):II32-8.
15. Saccani S, Nicolini F, Beghi C, Marcato C, Uccelli M, Larini P, et al. Thoracic aortic stents: a combined solution for complex cases. Eur J Vasc Endovasc Surg 2002; 24:423-7.
16. Vos AW, Linsen MA, Wisselink W, Rauwerda JA. Endovascular grafting of complex aortic aneurysms with a modular side branch stent-graft system in a porcine model. Eur J Vasc Endovasc Surg 2004;27:492-7.
17. Schneider DB, Curry TK, Reilly LM, Kang JW, Messina LM, Chuter TA. Branched endovascular repair of aortic arch aneurysm with a modular stent-graft system. J Vasc Surg 2003;38:855.
18. Bleyn J, Schol P, Vanbandenhove I, Vercaeren P. Side-branched modular endograft system for thoracoabdominal aortic aneurysm repair. J Endovasc Ther 2002;9:838-41.
19. Inoue K, Hosokawa H, Iwase T, Sato M, Yoshida Y, Ueno K, et al. Aortic arch reconstruction by transluminally placed endovascular branched stent graft. Circulation 1999;100(Suppl):II316-21.
20. Inoue K, Iwase T, Sato M, Yoshida Y, Tanaka T, Kubota Y, et al. Clinical application of transluminal endovascular graft placement for aortic aneurysms. Ann Thorac Surg 1997;63:522-8.
21. Inoue K, Sato M, Iwase T, Yoshida Y, Tanaka T, Tanaki S, et al. Clinical endovascular placement of branched graft for type B aortic dissection. J Thorac Cardiovasc Surg 1996;112:1111-3.
22. Imai Y, Urayama S, Uyama C, Inoue K, Ueno K, Kuribayashi S, et al. A system for computer-assisted design of stent-grafts for aortic aneurysms using 3-D morphological models. Cardiovasc Intervent Radiol 2001; 24:277-9.
23. Okada K, Shinoka S, Ishikawa T, Sato H, Kuji T, Tomino T. A case report of aneurysm of the diverticulum of the ductus arteriosus. Kyobu Geka 1993;46:1144-7.
24. Hattori T, Hirata K, Shimizu S. Aneurysm of the diverticulum of the ductus arteriosus. Nippon Kyobu Geka Gakkai Zasshi 1994;42:150-5.
25. Shichijo T, Suchiro K, Sakakibara H, Okada M, Yoshida H, Ohba O. A case report of aneurysm of the diverticulum of the ductus arteriosus in the elderly. Kyobu Geka 1994;47:299-301.
26. Jinno T, Tago M, Yoshida H, Yamane M. Aneurysm of the diverticulum of the ductus arteriosus in the adult with left pneumonectomy: report of a case. Kyobu Geka 2002;55:803-6.

Submitted May 17, 2004; accepted Aug 31, 2004.

CORRECTION

In: "Flow-induced neointimal regression in baboon polytetrafluoroethylene grafts is associated with decreased cell proliferation and increased apoptosis" (Berceli SA, Davies MG, Kenagy RD, and Clowes AW. J Vasc Surg 2002;36:1248-55).

On page 1251, in the "Results" portion of the "Materials and Methods" section, Fig 1, *C* is incorrect. The black and white bars representing high and low flow were reversed. The following is the correct figure:

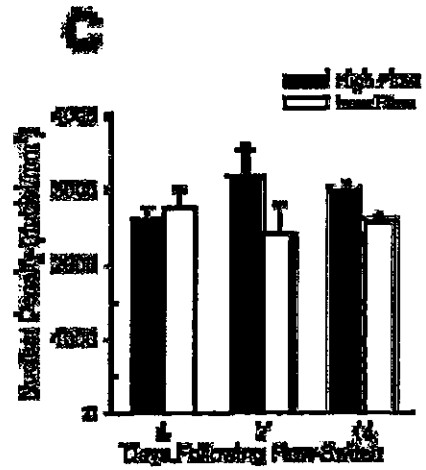

Fig 1. Neointimal SMC proliferation (BrdU labeling index; **A**), apoptosis (TUNEL labeling index; **B**), and nuclear density (**C**) in normal-flow and high-flow grafts after fistula placement. Values are mean ± standard error of mean.

THE JOURNAL OF BIOLOGICAL CHEMISTRY
Vol. 279, No. 14, Issue of April 2, pp. 14201–14206, 2004
Printed in U.S.A.

Type IV Collagen Is Transcriptionally Regulated by Smad1 under Advanced Glycation End Product (AGE) Stimulation*

Received for publication, September 22, 2003, and in revised form, January 15, 2004
Published, JBC Papers in Press, January 19, 2004, DOI 10.1074/jbc.M310427200

Hideharu Abe‡, Takeshi Matsubara§, Noriyuki Iehara¶, Kojiro Nagai§, Toshikazu Takahashi‡, Hidenori Arai§, Toru Kita‖, Toshio Doi‡**

From the ‡Department of Clinical Biology and Medicine, Course of Biological Medicine, University of Tokushima, Tokushima 770-8503, Japan and the Departments of §Geriatric Medicine, ¶Artificial Kidney, and ‖Cardiovascular Medicine, Kyoto University Graduate School of Medicine, Kyoto 606-8507, Japan

Prolonged exposure to hyperglycemia is now recognized as the most significant causal factor of diabetic complications. Excessive advanced glycation end products (AGEs) as a result of hyperglycemia in tissues or in the circulation may critically affect the progression of diabetic nephropathy. In diabetic nephropathy, glomerulosclerosis is a typical pathologic feature characterized by the increase of the extracellular matrix (ECM). We have reported previously that α1 type IV collagen (Col4) is one of the major components of ECM, which is up-regulated by AGEs, and that the overexpression of Col4 is transcriptionally regulated by an unknown transcription factor binding to the promoter. Here we identified this protein as Smad1 by yeast one-hybrid screening. Using chromatin immunoprecipitation and reporter assay, we observed that Smad1 directly regulated transcription for Col4 through the binding of Smad1 to the promoter of Col4. Smad1 was significantly induced along with Col4 in AGE-treated mesangial cells. Moreover, suppression of Smad1 by antisense morpholino resulted in a decrease of AGE-induced Col4 overproduction. To elucidate the interaction between transforming growth factor-β and Smad1, we investigated whether activin receptor-liked kinase1 (ALK1) was involved in this regulation. AGE stimulation significantly increased the expression of the ALK1 mRNA in mesangial cells. We also demonstrated that Smad1 and ALK1 were highly expressed in human diabetic nephropathy. These results suggest that the modulation of Smad1 expression is responsible for the initiation and progression of diabetic nephropathy and that blocking Smad1 signaling may be beneficial in preventing diabetic nephropathy and other various diabetic complications.

Diabetic nephropathy is the leading cause of end-stage renal disease and a major contributing cause of morbidity and mortality in patients with diabetes throughout the world. There is accumulating evidence that AGEs[1] have a pathogenic role in the development of diabetic glomerulosclerosis. Excessive AGEs produced as the result of hyperglycemia are known to stimulate the production of the ECM and inhibits its degradation. AGEs have a wide range of chemical, cellular, and tissue effects through changes in charge, solubility, and conformation that characterize molecular senescence. AGEs induce a variety of cellular events in vascular cells and other cells, possibly through several functional AGE receptors, thereby modulating the disease processes (1–5). AGEs have recently been accepted as having an important role, not only in diabetic complications but also in aging and old age-related diseases, including atherosclerosis (6, 7). Moreover, a truncated, soluble form of the receptor for AGEs was reported to suppress the development of accelerated diabetic atherosclerosis (8). Exposure of cultured mesangial cells to AGEs results in a receptor-mediated up-regulation of mRNA and protein secretion of Col4 (5, 9). However, there is little information regarding the mechanisms that underlie this regulation.

It was recently shown that TGF-β plays an important role in the AGE response of the glomeruli (10). Transgenic mice overexpressing TGF-β develop severe glomerulosclerosis (11). Thus, TGF-β is a central mediator of the sclerosing process in diabetic nephropathy. Members of the TGF-β superfamily bind to two different types of serine/threonine kinase receptors, termed type I and type II receptors (12). Type II receptors activate type I receptors, and signals are mediated through the type I receptors. Ligand-specific Smads are direct substrates of type I receptor kinases. Thus, the specificity of the signals is determined by type I receptors. ALK1 is one of the type I receptor members for TGF-β family proteins and has been linked to the inherited multisystemic vascular disorder, hereditary hemorrhagic telangiectasia 2 (HHT2). Although ALK1 has been known as an orphan receptor, recent reports show that ALK1 transduces TGF-β signals via Smad1 (13, 14).

Morphologically, the development of diabetic nephropathy is characterized by progressive thickening of the glomerular basement membrane (GBM) and, by expansion, of the mesangial ECM. During the process of glomerular injuries, mesangial cells can overproduce Col4 and secrete type I collagen (Col1) and osteopontin (OPN), which are not normally present in the mesangial matrix (15). In particular, Col4 is a major component of the thickened GBM and expanded ECM, but no molecules that directly regulate the Col4 expression have been found. The 130-bp bidirectional promoter of Col4 contains a large stem-loop structure (CIV), which has been shown to interact with several DNA-binding proteins (16). Using a gel mobility shift assay, we reported previously that an unknown protein binding to the CIV site directly regulates Col4 expression only when exposed to AGEs (9). To identify the protein that binds to the CIV site in the promoter region of the mouse *Col4* gene, we constructed a cDNA library from mouse mesangial cells treated with AGEs. In this study, we used a yeast one-hybrid system to isolate a clone that encodes a specific transcription factor from the library, and we identified the clone as the cDNA that encodes Smad1.

* This work was supported by Grant-in Aid from the Ministry of Education, Science, Sports and Culture of Japan. The costs of publication of this article were defrayed in part by the payment of page charges. This article must therefore be hereby marked "*advertisement*" in accordance with 18 U.S.C. Section 1734 solely to indicate this fact.

** To whom correspondence should be addressed. Tel.: 81-88-633-7184; Fax: 81-88-633-9245; E-mail: doi@clin.med.tokushima-u.ac.jp.

[1] The abbreviations used are: AGE, advanced glycation end product; ALK1, activin receptor-liked kinase1; AS, antisense; BMP, bone morphogenetic protein; BSA, bovine serum albumin; Col1, type I collagen; Col4, α1 type IV collagen; ECM, extracellular matrix; GBM, glomerular basement membrane; OPN, osteopontin; pSmad1, phosphorylated Smad1; TGF, transforming growth factor

EXPERIMENTAL PROCEDURES

Cell Culture—A glomerular mesangial cell line was established from glomeruli isolated from normal, 4-week-old mice (C57BL/6JrSJL/J) and was identified according to the method described previously (17). The mesangial cells were maintained in B medium (a 3:1 mixture of minimal essential medium/F12 modified with trace elements) supplemented with 1 mM glutamine, penicillin at 100 units/ml, streptomycin at 100 mg/ml, and 20% fetal calf serum. The cultured cells fulfilled the criteria generally accepted for glomerular mesangial cells previously (17). AGE or bovine serum albumin (BSA) exposure was carried out as described previously (9).

Preparation of AGEs—AGE-BSA was prepared by incubating BSA in phosphate-buffered saline (10 mM, pH 7.4) with 50 mM glucose 6-phosphate for 8 weeks at 37 °C as described previously (5). Unmodified BSA was incubated under the same conditions without glucose 6-phosphate as control. Protein concentrations were measured by the Bradford method. All AGE-protein specific fluorescence intensities were measured at a protein concentration of 1 mg/ml. AGE-BSA and control BSA contained 61.3 and 8.31 units of AGE per milligram of protein, respectively.

cDNA Library Construction and Yeast One-hybrid Screening—We prepared cDNA from mouse mesangial cells exposed to AGEs and inserted it into the pGAD10 vector. Yeast one-hybrid screening was carried out according to the MATCHMAKER one-hybrid protocol (Clontech). Briefly, tandem repeats of the 27-bp sequence (5′-TTCCTCCCCT-TGGAGGAGCGCCGCCCG-3′; CIV-1) from the mouse type IV collagen gene were ligated into the yeast integration and reporter vector pHISi or pLacZi to generate pHISi-CIV-1 or pLacZi-CIV-1, respectively (18). Each pHISi-CIV-1 and pLacZi-CIV-1 reporter construct was linearized and integrated into the genome of competent yeast YM4271, sequentially. The resulting yeast cells with the integrated pHISi-CIV-1 and pLacZi-CIV-1 were used for one-hybrid screening with the AGE-stimulated mouse mesangial cell library. Positive colonies were selected on synthetic dropout −His/−Leu plates with 45 mM 3-amino-1, 2, 4-triazole (3-AT). To exclude false positive clones, we performed a β-galactosidase filter lift assay according to manufacturer's instructions (Clontech). Plasmids were rescued from selected blue yeast colonies and retransformed into *E. coli* DH5α.

Chromatin Immunoprecipitation Assay—Chromatin immunoprecipitation assays were performed essentially as described previously by Luo *et al.* (19). We used anti-Smad1 antibody, anti-Smad4 antibody (Santa Cruz Biotechnology), or normal control IgG at 4 °C overnight. PCR was performed with primers to amplify the region containing the CIV-1 motif. The 5′-primer was 5′-GGAGCTCCCCAATTTGTTG-3′, and the 3′ primer was 5′-CAGCCTCCGCCTCTTACC-3′. The resulting product was ~100 bp by agarose gel electrophoresis.

Reporter Assay—1.3×10^6 COS7 cells in 10% fetal bovine serum/Dulbecco's modified Eagle's medium were seeded into 6-well plates. Eight hours later, the cells were transfected with 750 ng of CIV-1-LacZ reporter construct along with either 750 ng of vector encoding wild type Smad1 or the mock vector and 75 ng of CMV-LUC (Firefly luciferase under the control of cytomegalovirus promoter) as an internal control. Transfection was performed with FuGENE6 transfection reagent (Roche Molecular Biochemicals) according to the manufacturer's instructions. Forty-eight hours later, the cells were harvested in reporter lysis buffer, and β-galactosidase and luciferase activities were then measured using the Luminescent β-galactosidase reporter system (BD Biosciences) and the luciferase reporter assay system from Promega. β-galactosidase results were normalized for luciferase activity.

RNase Protection Assay—Total RNA was isolated from mesangial cells using the TRIsol reagent (Invitrogen), and an RNase protection assay was performed as described previously (20). Briefly, the RNA probes were prepared by linearizing the PvuII fragment of Col4 from p1234, the ApaI fragment of Col1 from pGM101, and the EcoRI fragment of glyceraldehyde-3-phosphate dehydrogenase (GAPDH) from pMGAP1. In addition, mouse riboprobe for Smad1 (5′-GCAAGTTTT-GCGATGTGAGA-3′ and 5′-GCATCTTCCAGAGTGAAGCC-3′), ALK1 (5′-GAGTGTGGCGGTCAAGATTT-3′ and 5′-GGAGCCGTGTTCATGG-TAGT-3′), and osteopontin (5′-TGCACCCAGATCCTATAGCC-3′ and 5′-CCTCAGTCCATAAGCCAAGC-3′) were amplified by reverse transcription PCR. The PCR fragments were sequenced to confirm that they were the respective cDNAs and then were cloned into a pGEM-T plasmid. After digesting the plasmid with SacI, an antisense riboprobe was synthesized *in vitro* using T7 RNA polymerase. The RNA probes and the test RNA were hybridized overnight at 45 °C. RNase A (40 μg/ml) and RNase T1 (2 μg/ml) were added to each tube, and the tubes were incubated for 1 h at 30 °C. The RNase resistant fragments were analyzed by 5% polyacrylamide/8 M urea gel electrophoresis and autoradiography. The protected bands for each RNA probe had the same size as the coding sequence for the specific mRNA, thus providing evidence for their specificity, and were evaluated by densitometric analysis.

Western Blotting—Cultured mesangial cells were treated with AGEs or BSA for 72 h. Cells were harvested in sample buffer, resolved by SDS-polyacrylamide gel electrophoresis, transferred to nitro-cellulose membrane, subjected to Western blot using a 1:500 dilution of antibody for Smad1 and pSmad1 (Santa Cruz Biotechnology), and detected using an enhanced chemiluminescence detection system (Invitrogen).

Immunostaining of Cultured Cells—Cultured cells were fixed in 4% paraformaldehyde. The antibodies used were anti-Smad1 antibody, 1:100 (Santa Cruz Biotechnology), and anti-pSmad1, 1:100 (Calbiochem). An appropriate fluorescein isothiocyanate-conjugated secondary antibody was used for visualization, and imaging was done using a confocal laser microscope and a fluorescent microscope (Olympus).

Smad1 Morpholino Antisense Oligonucleotide—The antisense oligonucleotide used was a 25-nucleotide morpholino oligo (Genetools LLC) with the base composition 5′-CAAGCTGGTCACATTCATAGCGGCT-3′. A standard morpholino oligo with the base composition 5′-CAtGCTcGTCACATTCAaAGCcGCT-3′ (points of mismatch are shown by small letters) was used as a control. Microinjection of *in vitro* transcribed RNA was performed as described previously (21).

Histology—Histopathological studies were performed on human tissues. This study was in accordance with the Declaration of Helsinki, and we obtained approval from the institutional review board. All patients gave their informed written consent. Diabetic kidney specimens ($n = 5$) were obtained from renal biopsies. Control human tissue sections were obtained from normal renal cortex harvested from kidneys removed for renal malignancy. Tissues for analysis were sampled from the pole opposite the tumor. Cryopreserved kidney tissues were cut in 5-μm-thick sections and fixed in acetone for 5 min. Endogenous peroxidase activity was quenched by a 20-min incubation in the dark with 1% H_2O_2 in methanol. To eliminate nonspecific staining, sections were incubated with the appropriate preimmune serum for 20 min at room temperature, followed by incubation with primary antibodies anti-Smad1 (Santa Cruz Biotechnology) and anti-ALK1 (R&D Systems) antibodies.

RESULTS

Smad1 Is Identified as a Binding Protein to Col4—To identify the protein binds to the CIV site in the promoter region of the mouse *Col4* gene, we constructed a cDNA library from mouse mesangial cells treated with AGEs. We then used a yeast one-hybrid system to isolate a clone that encodes a specific transcription factor from the library. We identified this clone as the cDNA that encodes Smad1. Smad1 is well known for transducing the bone morphogenetic protein (BMP) signal (22) and is essentially important in the development of kidney (23). However, the expression of Smad1 is not detected in glomeruli in adult mouse (24).

To confirm the binding of Smad1 to the *Col4* promoter *in vivo*, we performed a chromatin immunoprecipitation assay. Precipitated DNA was purified, and the promoter of the *Col4* gene was detected by PCR. The anti-Smad1 antibody precipitated chromatin containing the CIV-1 site from cells stimulated with AGEs (Fig. 1). In contrast, considerably less binding was observed in BSA-exposed cells. We also detected Smad4 on the CIV-1 site (Fig. 1). These observations suggest that Smad1 and Smad4 can target the CIV motif in mesangial cells, especially when exposed to AGEs.

Smad1 Transcriptionally Regulates Col4 Expression—Next, we examined the transcriptional activity of the *Col4* gene by a reporter assay. We constructed a vector by fusing the *CIV-1* promoter in front of the LacZ reporter and then cotransfected

FIG. 1. **Binding of Smad1 to *Col4* promoter.** Chromatin immunoprecipitation was carried out with mesangial cells under treatment with AGEs (*A*) or BSA (*B*) using the indicated antibodies. PCR was performed using primers for the CIV-1 motif. After sonication, DNA from 10% of each sample was saved as input fraction (*Input*). One of three independent experiments is shown.

with a wild-type Smad1 vector in COS7 cells. First, we confirmed the expression of Smad1 by Western blot analysis (Fig. 2*a*). Phosphorylated Smad1 (pSmad1) was detected in cell lysates that had been tranfected with wild-type Smad1 vector. Cotransfection of the wild-type Smad1 resulted in an 18-fold increase in a relative β-galactosidase activity of Col4 compared with that of the vector alone (Fig. 2*b*, *mock*). The *CIV-1* promoter has a GC-rich sequence in its 3′ end, which has been identified as a binding site for Smad1 (25). We then constructed two mutant reporter plasmids, the deletion mutant of GC rich in CIV-1 (5′-TTCCTCCCCTTGGAGGA-3′; Mut1) and the trinucleotide substitution mutant of GC rich motif in CIV-1 (5′-TTCCTCCCCTTGGAGGAGC$_3$C$_4$G$_5$CCG-3′; Mut2) (points of mutation are shown by small, underlined letters). The promoter activities of Mut1 and Mut2 were reduced to 4.9- and 4.3-fold increase, respectively (data not shown). β-galactosidase activity was normalized to luciferase activity and standardized as fold changes relative to cells cotransfected with the mock vector. In contrast, mock had no effect on the β-galactosidase activity in cotransfected cells. These results suggest that Smad1 is significantly involved in the induction of *Col4* gene transcription.

Activation and Translocation of Smad1 under AGE Exposure—To determine whether Smad1 is transcriptionally up-regulated by AGEs, we examined the expression of Smad1 in mesangial cells with or without AGEs stimulation. The levels of Smad1 mRNA were proportionally increased in a time-dependent manner (Fig. 3*a*). Similarly, the levels of *Col4* mRNA increased in parallel with the up-regulation of Smad1 transcripts. After BSA treatment, however, no change in the mRNA expression of *Smad1* or *Col4* was detected. Smad1 is well known to be phosphorylated and translocated into the nucleus, where it participates in the transcriptional regulation of target genes (22, 26). Therefore, we next examined the issue of whether the phosphorylation and translocation of Smad1 is affected by AGE treatment in mesangial cells (Fig. 3*b*). Consistent with the RNase protection assay, Smad1 and pSmad1 were distributed throughout mesangial cells with a preferential cytoplasmic localization after a 72 h-incubation in the presence of AGEs. Furthermore, the nuclear accumulation of Smad1 and pSmad1 in response to AGEs was observed in the cells 120 h after AGE stimulation, whereas BSA treatment led to little expression of Smad1 and pSmad1. The cells were counterstained with DAPI, and the nuclei were identified (data not shown). Similarly, both the Smad1 and pSmad1 proteins were detected in extracts from AGE-treated, but not BSA-treated, cells (Fig. 3*c*). These findings indicate that the regulation of Col4 is correlated with the expression of Smad1 under AGE exposure.

The Blocking of Smad1 Attenuates ECM Protein Overproduction—To examine the importance of the Smad1 signaling pathway for the AGE-induced overexpression of Col4, we selectively inhibited this pathway by the antisense (AS) gene. The AGE-

FIG. 2. **Effects of Smad1 on Col4 transcriptional activity.** *a*, cells were cotransfected with CIV-1-lacZ reporter plasmid and with either the vector encoding wild-type Smad1 (*Smad1-Wt*) or the vector alone (*Mock*), along with CMV-LUC as an internal control. Whole cell lysates were analyzed by Western blot with the anti-Smad1 and anti-pSmad1 antibody. One of three independent experiments is shown. *b*, after 48 h, cells were lysed, and β-galactosidase (*β-gal*) and luciferase (*Luc*) activities were measured. Values are the averages of triplicate determinations ±S.D.

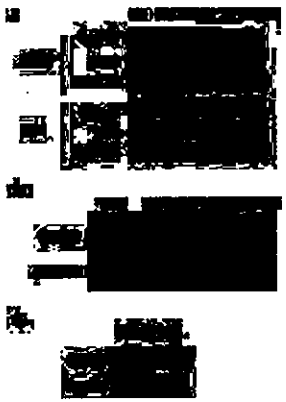

FIG. 3. **Exposure to AGEs causes dynamic changes in Smad1 expression.** *a*, RNase protection assay analysis of *Smad1* and *Col4* mRNA expression in total RNA lysates from mesangial cells treated with AGEs or BSA for the indicated time periods. Chronic stimulation of AGEs promotes *Smad1* continuous expression, paralleled with expression of *Col4*. One of three independent experiments is shown. Glyceraldehyde-3-phosphate dehydrogenase (*GAPDH*) was used as an internal control. *b*, immunofluorescence of mesangial cells after 72 or 120 h of treatment with AGEs or BSA. Data from one of three representative experiments is shown. *c*, Smad1 and pSmad1 were monitored by Western blot in response to a 72-h treatment with AGEs or BSA. One of three independent experiments is shown.

mediated induction of Smad1 was completely abolished in the presence of AS, but not in the presence of control oligos (4-mismatch) (Fig. 4, *a* and *b*). The overexpression of Col4 was strongly attenuated, consistent with the inhibition of Smad1. Similarly, both *Col1* and *OPN* mRNA levels were significantly

FIG. 4. **Effects of antisense oligo specific for Smad1 in mesangial cells.** *a*, immunofluorescence analysis of the antisense-treated mesangial cells, using the anti-Smad1 antibody (*green*) merged with DNA stained by DAPI (*blue*). After 72 h of incubation with AGEs, mesangial cells were incubated for 16 h in medium containing AS-Smad1 or 4-mismatch (*Control*). Data from one of three representative experiments is shown. *b*, Western blot analysis of Smad1 protein expression in mesangial cells treated with AGEs after transfection of AS or control. One of three independent experiments is shown. *c*, AS-Smad1 blocks the up-regulated mRNA levels of *Col4*, *osteopontin*, and *Col1* induced by AGEs treatment on mesangial cells. One of three independent experiments is shown.

decreased (Fig. 4*c*). Smad1 mismatch morpholino oligos (control) had no effect on the expression of these genes. These data indicate that Smad1 plays a critical role in the control of Col4 expression.

Smad1 and ALK1 Expression in Diabetic Conditions—To further elucidate the mechanism of Smad1 expression after AGE treatment, we investigated the expression of ALK1 in mesangial cells. ALK1 is a type I receptor for TGF-β family proteins and, specifically, phosphorylates Smad1 and Smad5. We were able to detect the significant increase in ALK1 mRNA expression in AGE-treated mesangial cells using an RNase protection assay (Fig. 5). In addition, at 10 μg/ml the TGF-β-neutralizing antibody significantly attenuated the up-regulated mRNA levels of *ALK1* and *Smad1* under AGE stimulation (data not shown). Furthermore, we examined whether high glucose exposure affected the expression of *ALK1*, *Smad1*, or *Col4*. In this condition, mRNA levels of these genes were increased, but they were weak and transient, compared with AGEs exposure (data not shown).

Finally, we investigated the glomerular expression of Smad1 and ALK1 in human diabetic nephropathy. We carried out indirect immunohistochemistry on renal biopsies (diabetic nephropathy) and on normal kidney tissue. Glomerular im-

FIG. 5. **Regulation of ALK1 mRNA expression by AGEs.** After treatment with AGEs, the specific mRNAs were determined by using the RNase protection assay. The amount of total RNA loaded (1 μg/lane) was checked by hybridization with a glyceraldehyde-3-phosphate dehydrogenase (*GAPDH*) probe. The data are representative of three independent experiments.

munoreactivity for Smad1 and ALK1 was correlated with the severity of sclerotic lesions in diabetic renal glomeruli; the immunoreactive signal was nearly absent in normal glomeruli (Fig. 6). These histological observations suggest that the ALK1/Smad1 signaling pathway is linked to the ECM expansion.

DISCUSSION

Changes in GBM structure occur very earlier in diabetic nephropathy, even before microalbuminuria is apparent. Although Col4 is the principal component of the GBM, the cellular and molecular mechanisms involved in the up-regulation of Col4 in diabetic conditions are, as yet, poorly understood. We have reported previously that an unknown protein binds to the Col4 promoter under AGE exposure (9). Here, we identified the protein as Smad1 using a yeast one-hybrid system. It is generally acknowledged that Smad1 transduces BMP signals, inducing formation of bone and cartilage (22). Moreover, signaling by Smad1 is modulated by various other proteins such as signal transducers and activators of transcription 3 (STAT3) (27) and Smurf1 (28), allowing the TGF-β superfamily ligands to elicit diverse effects on target cells. Recently, mesangial cells have been shown to produce TGF-β when exposed to AGEs (29). We observed that chronic exposure of AGEs, inducing the sustained increase in *Smad1* gene activation and expression, leads to Col4 overproduction, suggesting that Smad1 is a critical modulator in diabetic conditions.

Targeted gene disruption of the *Smad1* gene in mice results in embryonic lethality, suggesting that Smad1 plays critical roles in early embryogenesis (30). However, because of the early embryonic lethality, not much is known about the role of Smad1 *in vivo*, particularly in the adult. A recent study has shown that Smad1 is absent in renal glomeruli in normal adult mouse (24). We show for the first time that AGEs induce the expression of Smad1 in adult mouse glomeruli. Therefore, Smad1 may be the earliest indicator of renal dysfunction.

Development of diabetic kidney disease in diabetic patients is a huge clinical problem associated with increased morbidity and mortality. It is also clear that the current therapy, optimal glycemic control, can slow (1, 2) but not prevent the development or progression of diabetic nephropathy in most patients. Previous studies have shown that TGF-β is a key mediator of ECM accumulation in experimental and human kidney disease, leading to progressive glomerular scarring and renal failure (10, 11). Therapeutic approaches to down-regulate TGF-β signaling under diabetic conditions provide one strategy for inhibiting the progression of diabetic nephropathy. For example, the use of the endogenous proteoglycan decorin (natural inhibitor of TGF-β) (31) and the use of a neutralizing TGF-β antibody (32) have been shown to prevent the development of diabetic glomerulosclerosis. However, prolonged inhibition of TGF-β may lead to unwanted adverse effects, because TGF-β has anti-proliferative effect in some cancers and, in one report, Smad3-deficient animals found metastatic colon tumors (33). Therefore, inhibitors for specific responses of TGF-β will lead to

FIG. 6. **Detection of Smad1 and ALK1 in human diabetic kidney.** Immunohistochemical staining of glomeruli from kidneys of diabetic (*DM*; $n = 5$) or non-diabetic (*non-DM*; $n = 3$) patients stained with anti-Smad1 and anti-ALK1 antibodies. Glomerular positivity of Smad1 and ALK1 was prominently detectable in diabetic patients but not detectable in non-diabetic patients. All sections were counterstained with hematoxylin. Original magnification for all was ×400.

a novel therapeutic approach. We have demonstrated here that the morpholic antisense oligo specific for Smad1 strongly attenuated the overproduction of Col4 induced by AGEs. Similarly, Col1 and OPN mRNA expressions were partially inhibited. It is reported that Smad1 dissociates the repressor Hoxc-8 from the *OPN* promoter, thereby inducing *OPN* transcription (34). Thus, Smad1 may be a novel therapeutic target in diabetic complications and be useful in combination with the current therapy.

TGF-β evokes its biological effects by signaling through two different types of serine/threonine kinase receptors. Type II receptor activates type I receptors, which transduce various signals via the Smads (22, 26). Recent reports demonstrated that ALK1 has been thought of as a BMP signal transducer, mediating signals from TGF-β via Smad1 (13, 14). Therefore, we investigated the expression of ALK1 in mouse mesangial cells and human kidney tissues. We have also shown that ALK1 and Smad1 are expressed in renal glomeruli, corresponding to the progression of diabetic conditions. These results lead not only to a better understanding of the mechanisms responsible for the initiation and progression of diabetic conditions but also to the development of novel therapeutic strategies for the treatment of diabetic complications in various organs by suppressing the pathologically activated production of collagen. Both Smad1 and ALK1 are nearly absent in normal mesangial cells. In this study, we first demonstrated that ALK1 as well as Smad1 participate in the development of diabetic change in kidney, suggesting that ALK1 acts upstream of the excessive production of Col4.

AGEs are known to induce a variety of cellular events in vascular cells and other cells, possibly through the functional several AGEs receptors, thereby modulating the disease processes. AGEs have been recently accepted as having an important role, not only in diabetic complications but also in aging and old age-related diseases, including atherosclerosis (6, 7). Col4 is also a major component of the vascular basement membrane that lies beneath the endothelium, surrounds medial smooth muscle cells, and undergoes significant nonenzymatic glycosylation (glycation). Glycation leads ultimately to increased cross-linking of collagen, resulting in increased arterial stiffness (35). We report here that AGE-induced Col4 overproduction is mediated by Smad1 signaling. Recent reports show that Smad1 is expressed in endothelial cells of some blood vessels and is at the site of vasculogenesis in the developing yolk sac during blood island formation (36). Furthermore, ALK1 is highly expressed in vascular endothelial cells (22, 37) and may be essential for vascular maturation and stabilization (38, 39). Inactivating mutations of ALK1 result in human hereditary hemorrhagic telangiectasia 2, also known as Osler-Rendu-Weber syndrome (40). In addition, recent evidence indicates that Smad1 transcriptionally regulates the osteopontin gene (33), which is a key factor of the progression of renal injuries and atherosclerosis. Accordingly, we speculate that the ALK1/Smad1 signaling may mediate the development of atherosclerosis, both in diabetic patients and in the aged, by inducing an overproduction of ECM. Because diabetic renal disease in the human is a process that occurs slowly over many years, it is likely that a very detailed evaluation of this phenomenon will be required to determine the interaction of Smad1 and ALK1 in this condition. Further work is in progress to clarify the role of ALK1/Smad1 in diabetic kidney using animal models.

Acknowledgments—We thank Dr. K. Miyazono (The University of Tokyo, Japan) for providing a plasmid encoding Smad1 and Dr. Y. Takishita (Tokushima Prefectural Central Hospital, Japan) for his assistance with histological analysis. We also thank the members of our laboratory for discussions.

REFERENCES

1. The Diabetes Control and Complications Trial Research Group (1993) *N. Engl. J. Med.* **329**, 977–986
2. United Kingdom Prospective Diabetes Study (UKPDS) Group (1998) *Lancet* **352**, 837–853
3. Vlassara, H., Striker, L. J., Teichberg, S., Fuh, H., Li, Y. M., and Steffes, M. (1994) *Proc. Natl. Acad. Sci. U. S. A.* **91**, 11704–11708
4. Brownlee, M., Cerami, A., and Vlassara, H. (1988) *N. Engl. J. Med.* **318**, 1315–1321
5. Doi, T., Vlassara, H., Kirstein, M., Yamada, Y., Striker, G. E., and Striker, L. J. (1992) *Proc. Natl. Acad. Sci. U. S. A.* **89**, 2873–2877
6. Vlassara, H., Fuh, H., Makita, Z., Krungkrai, S., Cerami, A., and Bucala, R. (1992) *Proc. Natl. Acad. Sci. U. S. A.* **89**, 12043–12047
7. Huijberts, M. S., Wolffenbuttel, B. H., Boudier, H. A., Crijns, F. R., Kruseman, A. C., Poitevin, P., and Levy, B. I. (1993) *J. Clin. Investig.* **92**, 1407–1411
8. Park, L., Raman, K. G., Lee, K. J., Lu, Y., Ferran, L. J., Jr., Chow, W. S., Stern, D., and Schmidt, A. M. (1998) *Nat. Med.* **9**, 1025–1031
9. Ishara, N., Takeoka, H., Yamada, Y., Kita, T., and Doi, T. (1996) *Kidney Int.* **50**, 1166–1172
10. Yang, C. W., Vlassara, H., Peten, E. P., He, C. J., Striker, G. E., and Striker, L. J. (1994) *Proc. Natl. Acad. Sci. U. S. A.* **91**, 9436–9440
11. Sanderson, N., Factor, V., Nagy, P., Kopp, J., Kondaiah, P., Wakefield, L., Roberts, A. B., Sporn, M. B., and Thorgeirsson, S. S. (1995) *Proc. Natl. Acad. Sci. U. S. A.* **92**, 2572–2576
12. ten Dijke, P., Miyazono, K., and Heldin, C. H. (1996) *Curr. Opin. Cell Biol.* **8**, 139–145
13. Oh, S. P., Seki, T., Goss, K. A., Imamura, T., Yi, Y., Donahoe, P. K., Li, L., Miyazono, K., ten Dijke, P., Kim, S., and Li, E. (2000) *Proc. Natl. Acad. Sci. U. S. A.* **97**, 2626–2631
14. Chen, Y. G., and Massague, J. (1999) *J. Biol. Chem.* **274**, 3672–3677
15. Floege, J., Johnson, R. J., Gordon, K., Iida, H., Pritzl, P., Yoshimura, A., Campbell, C., Alpers, C. E., and Couser, W. G. (1991) *Kidney Int.* **40**, 477–488
16. Bruggeman, L. A., Burbelo, P. D., Yamada, Y., and Klotman, P. E. (1992) *Oncogene* **7**, 1497–1502
17. Davies, M. (1994) *Kidney Int.* **45**, 320–327
18. Burbelo, P. D., Utani, A., Pan, Z. Q., and Yamada, Y. (1993) *Proc. Natl. Acad. Sci. U. S. A.* **90**, 11543–11547
19. Lee, R. K., Postigo, A. A., and Dean, D. C. (1998) *Cell* **94**, 463–473
20. Abe, H., Ishara, N., Utsumomiya, K., Kita, T., and Doi, T. (1999) *J. Biol. Chem.* **274**, 20874–20878
21. Ahn, D. G., Kourakis, M. J., Rohde, L. A., Silver, L. M., and Ho, R. K. (2002) *Nature* **417**, 754–758
22. Massagoe, J., and Wotton, D. (2000) *EMBO J.* **18**, 1745–1754
23. Roelen, B. A., van Rooijen, M. A., and Mummery, C. L. (1997) *Dev. Dyn.* **209**, 418–430
24. Huang, S., Flanders, K. C., and Roberts, A. B. (2000) *Gene* **258**, 45–53
25. Kusanagi, K., Inoue, H., Ishidou, Y., Mishima, H. K., Kawabata, M., and Miyazono, K. (2000) *Mol. Biol. Cell* **11**, 555–565
26. Heldin, C. H., Miyazono, K., and ten Dijke, P. (1997) *Nature* **390**, 465–471
27. Nakashima, K., Yanagisawa, M., Arakawa, H., Kimura, N., Hisatsune, T., Kawabata, M., Miyazono, K., and Taga, T. (1999) *Science* **284**, 479–482
28. Zhu, H., Kavsak, P., Abdollah, S., Wrana, J. L., and Thomsen, G. H. (1999) *Nature* **400**, 687–693
29. Throckmorton, D. C., Brogden, A. P., Min, B., Rasmussen, H., and Kashgarian, M. (1995) *Kidney Int.* **48**, 111–117
30. Tremblay, K. D., Dunn, N. R., and Robertson, E. J. (2001) *Development* **128**, 3609–3621
31. Isaka, Y., Brees, D. K., Ikegaya, K., Kaneda, Y., Imai, E., Noble, N. A., and Border, W. A. (1996) *Nat. Med.* **2**, 418–423
32. Chen, S., Carmen, Iglesias-de la Cruz, M., Jim, B., Hong, S. W., Isono, M., and Ziyadeh, F. N. (2003) *Biochem. Biophys. Res. Commun.* **300**, 16–22
33. Zhu, Y., Richardson, J. A., Parada, L. F., and Graff, J. M. (1998) *Cell* **94**, 703–714
34. Shi, X., Yang, X., Chen, D., Chang, Z., and Cao, X. (1999) *J. Biol. Chem.* **274**, 13711–13717
35. Chappey, O., Dosquet, C., Wautier, M. P., and Wautier, J. L. (1997) *Eur. J. Clin. Investig.* **27**, 97–108
36. Dick, A., Risau, W., and Drexler, H. (1996) *Dev. Dyn.* **211**, 293–305
37. Attisano, L., Carcamo, J., Ventura, F., Weis, F. M., Massague, J., and Wrana, J. L. (1993) *Cell* **75**, 671–680
38. Urness, L. D., Sorensen, L. K., and Li, D. Y. (2000) *Nat. Genet.* **26**, 328–331
39. Larsson, J., Goumans, M. J., Sjostrand, L. J., van Rooijen, M. A., Ward, D., Levesn, P., Xu, X., ten Dijke, P., Mummery, C. L., and Karlsson, S. (2001) *EMBO J.* **20**, 1663–1673
40. Johnson, D. W., Berg, J. N., Baldwin, M. A., Gallione, C. J., Marondel, I., Yoon, S. J., Stenzel, T. T., Speer, M., Pericak-Vance, M. A., Diamond, A., Guttmacher, A. E., Jackson, C. E., Attisano, L., Kucherlapati, R., Porteous, M. E., and Marchuk, D. A. (1996) *Nat. Genet.* **13**, 189–195

Late Restenosis of the Balloon-Dilated Site
—— Serial Angiographic Observations Beyond 7 Years ——

Takashi Yamada, MD; Katsumi Inoue, MD; Naoya Hamasaki, MD; Yoshihisa Nakagawa, MD; Masashi Iwabuchi, MD; Hiroyoshi Yokoi, MD; Takeshi Kimura, MD; Hideyuki Nosaka, MD; Masakiyo Nobuyoshi, MD

Background The present retrospective study was performed to assess the long-term (>7 years) fate of stabilized balloon-dilated sites.

Methods and Results Between February and April 1986, 171 patients underwent successful percutaneous balloon angioplasty. Early restenosis (<1 year) occurred in 53%, but repeat balloon angioplasty stabilized the balloon-dilated site. The early period was defined as 6 months, late years as 3–5 years and long-term years as 7–12 years. Angiographic evaluation at both early year or late year periods (mean=4.7 years) and long-term (mean=10.4 years) periods following stabilization was available in 71 patients (94 lesions) with mean age of 61.7±8.5 years. Of the 71 patients 69.6% were male. Restenosis occurring after 1 year was defined as late restenosis. The mean diameter stenosis changed from 6 months (50.3±12.4%) to late-period (44.2±13.2%; $p<0.05$) and long-term period (50.3±16.1%; $p<0.001$); but the reference vessel diameter did not change significantly. Late restenosis occurred in 28% (3–5 years) and 33% (7–12 years) of 94 lesions, and 13.8% of lesion required repeat target lesion revascularization. During this period, 5.3% of patients (5 lesions) underwent revascularization for new proximal or distal lesions.

Conclusions Decrease of luminal diameter during the early 6 months, was followed by regression after stabilization of the balloon-dilated site up to 5 years, but luminal re-narrowing occurs again over 7 years after balloon angioplasty. (*Circ J* 2005; **69**: 380–385)

Key Words: Angioplasty; Coronary disease; Follow-up studies; Restenosis

Percutaneous coronary balloon angioplasty (PTBA) has become a popular alternative to bypass surgery as a less invasive revascularization therapy for chronic coronary artery disease (CAD) since the 1980s. However, published documents have been reported where a high percentage of patients with occuring restenosis within 6 months of angioplasty and this has limited its use![1–10] Early clinical investigations reported that restenosis rarely occurs beyond 6 to 12 months after balloon angioplasty. Experimental studies in a number of species have shown that the initial myointimal thickening response composed of proliferation of smooth muscle cells and extracellular matrix to injury reaches a maximum within a few months; in the absence of further injury, luminal enlargement ensues reported as 'late regression'![1] Further angiographic investigations have reported preservation of balloon-dilated site for a decade if the patient is stable after 6 months after balloon angioplasty![12] In contrast, our pathological findings suggest that atherosclerosis progresses again after 7 years from balloon angioplasty.

In the present study, we report re-progression after late regression occurring more than 7 years after balloon angioplasty.

(Received August 9, 2004; revised manuscript received December 6, 2004; accepted January 12, 2005)

Department of Cardiology, Kokura Memorial Hospital, Kitakyushu, Japan

Mailing address: Masakiyo Nobuyoshi, MD, Department of Cardiology, Kokura Memorial Hospital, 1-1 Kifune-machi, Kokurakita-ku, Kitakyushu 802-8555, Japan. E-mail: kmhptca@nn.iij4u.or.jp

Methods

Patient Population

Between February and April 1986, 203 consecutive patients underwent clinically uneventful coronary balloon angioplasty for de novo native coronary artery lesions at Kokura Memorial Hospital, Kitakyushu, Japan. According to angiographic criteria (>20% increase of minimal luminal diameter by visual estimation) and clinical criteria (improvement of symptom status without major complications), the procedure was considered successful in 171 patients (84.2%). Angiographic follow-up studies at 6 months (0.6 years=early), 3–5 years (4.7 years=late) and beyond 7 years (7–12 years; 10.4 years=long-term) in 71 (41.5%) patients with 94 lesions (group A), 23 of whom were followed up to 15 years, were available for retrospective analysis. Lesions with restenosis that were amenable to conservative treatment or restenosis treated by repeat angioplasty within 1 year after balloon angioplasty were eligible for enrollment in the study. Lesions with no need for bypass surgery, repeat-balloon angioplasty or death for 1 year were defined as 'stabilized'.

Follow-up Angiography

Coronary angiography at the early, late and long-term periods after PTBA was performed regardless of symptoms in these 71 patients. Quantitative angiographic analysis was performed with the Cardiovascular Angiography Analysis System II. Minimal lesion lumen diameter and lesion length was measured; percentage diameter stenosis as well as the interpolated reference diameter was calculated. Care was taken by the operator to select the same reference points for the post-intervention and follow-up studies. The minimal lumen diameter was determined by computer at the same ballooned site taking the most severe narrowing, even if it was far from the initial narrowest point providing it was within the balloon-dilated site. The measurements of 2 angiographic views were averaged. Isosorbide dinitrate (5 mg) was injected intracoronally before each angiography. The diameter of 5F to 8F catheter tips free of contrast medium filmed at the center of the image were caliper measured and used for calibration in each study. Early restenosis was defined as more than 50% diameter stenosis observed at the 6-month angiography; late restenosis (LR) was defined as restenosis occurring beyond 1 year after angioplasty.

Statistical Analysis

Continuous variables are expressed as mean±1SD and compared with paired t-test for matched observations, or unpaired t-test if non-matched. Categorical variables were compared by the chi-square or Fisher's exact test. All tests of significance were two-tailed, and p-values of less than 0.05 were considered to be statistical significant. A change of stenosis diameter by >0.5 mm was defined as significant between late and long-term periods.

Results

Patient Characteristics

Seventy-one of 171 patients (group A) had follow-up angiography beyond 7 years, 23 of whom were followed beyond 12 years (Table 1), but in 74 patients (group B) angiography beyond 7 years was not available. Table 2 describes and compares the baseline characteristics of both groups.

There were no significant differences between the 2 groups. Follow-up angiography of group A patients showed: (i) early period at a mean of 7.2 months (range: 1.5 to 11.6 months); (ii) late or 3–5 years at 4.7 years (range: 2.9 to 6.3 years) after stabilization; and (iii) long-

Table 1 Derivation of the Study Patients (Serial Late Angiographic Follow-up)

First time balloon angioplasty in 1986 (n=203)	
Unsuccessful	*19*
CABG	*7*
Death	*6*
Successful (n=171)	
Angiographic follow-up beyond 7 years (study group) (n=71)	
Angiographic follow up <7 years	*74*
CABG <7 years	*12*
Death <7 years	*13*
TLR after stabilization <7 years	*1*
Total (n=71)	*100*

CABG, coronary artery bypass graft; TLR, target lesion revascularization.

Table 3 Symptomatic Status at Late and Long-Term Angiographic Follow-up Period

	Late (n=71)	*%*	*Long-term (n=71)*	*%*
Asymptomatic	*43*	*60.6*	*29*	*41.4*
Symptomatic	*28*	*39.4*	*41*	*58.6*
CCS 3/4	*12*	*16.9*	*19*	*27.1*
Acute MI	*1*	*1.4*	*3*	*4.3*
Vasospasm	*2*	*2.8*	*0*	*0.0*
New leison related	*25*	*35.2*	*24*	*34.3*
Balloon-dilated lesion related	*1*	*1.4*	*9*	*12.9*
Unclear	*0*	*0.0*	*8*	*11.4*

CCS, angina classification of Canadian Cardiovascular Society; MI, myocardial infarction.

Table 2 Baseline Characteristics of Group A Study Group Patients and Group B Patients Without Late Angiographic Follow-up

	Group A	*%*	*Group B*	*%*	*p value*
Patients	*71*		*74*		
Lesions	*94*		*105*		
Old MI	*40*	*56.3*	*33*	*44.6*	*0.14*
CCS 3/4	*27*	*38.0*	*33*	*44.6*	*0.25*
Multivessel disease	*32*	*45.1*	*38*	*51.4*	*0.39*
Acute MI	*12*	*16.9*	*8*	*10.8*	*0.47*
Target vessel					
LAD	*37*	*39.4*	*45*	*42.9*	
LCX	*32*	*34.0*	*30*	*28.6*	
RCA	*25*	*26.6*	*29*	*27.6*	
LMT	*0*	*0.0*	*1*	*1.0*	
Poor LVEF	*2*	*2.8*	*2*	*2.7*	*0.99*
Age	*61.7±8.5*		*62.9±8.9*		*0.36*
Male	*49*	*69.0*	*51*	*68.9*	*0.99*
Hypertension	*30*	*42.3*	*25*	*33.8*	*0.30*
Hyperlipidemia	*17*	*23.9*	*21*	*28.4*	*0.58*
Diabetes mellitus	*15*	*21.1*	*15*	*20.3*	*0.86*
Smoking	*28*	*39.4*	*30*	*40.5*	*0.89*
Total cholesterol	*189±59*		*192.1±42*		*0.73*
Triglycerides	*143.2±83*		*137.1±60*		*0.61*
High-density cholesterol	*41.1±18*		*42.1±16*		*0.35*
HbA1c	*5.96±1.8*		*5.97±1.6*		*0.98*
Creatinine	*1.38±1.6*		*1.20±0.2*		*0.56*
TLR <1 year	*18*	*25.4*	*16*	*21.6*	*0.49*

MI, myocardial infarction; CCS, angina classification of Canadian cardiovascular society; LAD, left anterior descending coronary artery; LCX, left circumflex coronary artery; RCA, right coronary artery; LMT, left main trunk; HbA1c, Hemoglobin A1c.

Table 4 Quantitative Coronary Angiographic Analysis at Various Follow-up Periods

	Pre (n=94)	Immediate (n=94)	Early 6 months (n=94)	Late 3–5 years (n=94)	Long-term 7–12 years (n=94)	Long-term 12–15 years (n=23)
Minimal lumen diameter, mm	0.75±0.32	1.49±0.39	1.38±0.43	1.54±0.45	1.41±0.54	1.24±0.54
p-value	<0.0001	0.0671	<0.0001	0.0007	0.0862	
Reference diameter, mm	2.74±0.56	2.72±0.57	2.77±0.59	2.76±0.51	2.79±0.58	2.48±0.51
p-value	0.1254	0.9734	0.9815	0.4192	0.2345	
Diameter stenosis, %	70.9±11.4	48.9±11.3	50.7±12.1	44.2±13.2	51.6±16.9	48.7±18.9
p-value	<0.0001	0.3839	<0.0001	0.0005	0.573	
Lesion length, mm	13.1±8.3	10.7±4.9	12.1±6.4	10.9±4.6	11.4±6.3	11.7±7.2
p-value	0.0016	0.1453	0.0295	0.526	0.2553	
%Diameter stenosis >50	100%	33%	52%	28%	33%	48%

Statistical analysism paired t-test used.

Table 5 Need of Repeat Percutaneous Coronary Intervention (PCI) Beyond 7 Years Post-Stabilization

	n=94	%
LR at long-term	31	33.0
LR (%DS >70)	11	11.7
Total occlusion at long-term	7	7.4
AMI	3	3.2
Silent occlusion	2	2.1
Proximal total occlusion	2	2.1
PCI of new lesion in non-dilated vessel	25	26.6
PCI of same vessel	18	19.1
PCI of LR	13	13.8
PCI of new proximal or distal lesion	5	5.3
Proximal	3	3.2
Distal	2	2.1

LR, late restenosis; %DS, percentage diameter stenosis.

term or beyond 7 years between 6.9 to 11.8 years after stabilization, or 12 to 14.6 years for the subgroup of 23 patients.

There were fewer symptomatic patients at the late follow-up period than at the long-term follow-up. The incidence of unstable angina and acute myocardial infarction was slightly more frequent at the long-term follow-up period. While the incidence of new lesion-related ischemia was the same for both late and long-term follow-up periods, balloon-dilated site-related ischemia was greater at the long-term period (Table 3). One patient required repeat angioplasty for LR by the late-follow-up period, and was therefore excluded from the long-term follow-up. Repeat percutaneous coronary interventions (PCI) were required for disease progression in 22 (31%) patients with 25 (27%) new lesions, and 13 (18%) patients with 13 (14%) late restenotic lesions.

Angiographic Results

The mean minimal lumen diameter attained at the initial balloon angioplasty decreased, although not significantly during the first 6 months, and subsequently increased up to the late follow-up period, but then decreased significantly to the long-term follow-up period. The derived parameters changed accordingly. In contrast the reference diameter remained practically unchanged (Table 4).

While the incidence of lesions with percentage diameter stenosis >50 decreased from the early to the late follow-up period, it increased significantly to the long-term period. This resulted in an LR rate of 26 lesions (28%) for the late period, and 31 lesions (33%) for the long-term follow-up, the stenosis being severe (percentage diameter stenosis >70) in 11 lesions (12%). Seven lesions resulted in total occlusion (Table 5).

Regression and Progression After Stabilization

There was significant lesion regression in 23 of 94 lesions (24.5%), while in 6 (6.4%) there was significant progression occurred up to the late follow-up period; thus regression being dominant during the first 5 years (Fig 1).

In contrast lesion-progression dominated at the long-term follow-up period and was observed in 22 patients (23.4%; Fig 2).

Discussion

Many clinical investigations have reported that restenosis in balloon-dilated sites mainly occurred during the first 6 months after successful angioplasty, and rarely beyond that time, for the phenomenon of regression occurrs thereafter up to 5 years[11,13–16] In a previous clinical study the stenotic diameter did not change significantly between 6 months and 10 years after angioplasty![12] The results from the present study confirmed the phenomenon of late regression up to 5 years after balloon angioplasty, but also late progression at 10 years. Interestingly lesions with more than 40% of diameter stenosis at the late follow-up time did not progress by the long-term period, but those with less than 40% progressed significantly with no further enlargement of vessel diameter, in contrast to the reported regression after 5 years of balloon angioplasty![11]

Our early restenosis rate of 52%, somewhat higher than published data[17–20] may be due to the relatively small mean luminal diameter of the dilated reference arteries (2.74± 0.56, n=94). However, there was no significant differences about patient characteristics between with and without late angiographic follow-up. Disease progression in CAD is an insidious phenomenon, but often responsible for the late recurrence of cardiac symptoms and events. Angioplasty per-se may trigger the appearance of a new lesion(s) proximal to the balloon-dilated site[21–23] Five (5.3%) of our study lesions needed repeat PCI. Three (60%) lesions were proximal, but 2 (40%) occurred in the same vessel, distal and unrelated to the dilated lesion several years after balloon angioplasty. Therefore, this indicates that this phenomenon may or may not be secondary to the endothelial injury by the guidewire or balloon catheter, but rather suggests disease progression.

A rigorous and quantitatively evaluated serial angiographic study at 1, 3, 6 and 12 months after angioplasty showed that most of the reduction in mean minimum

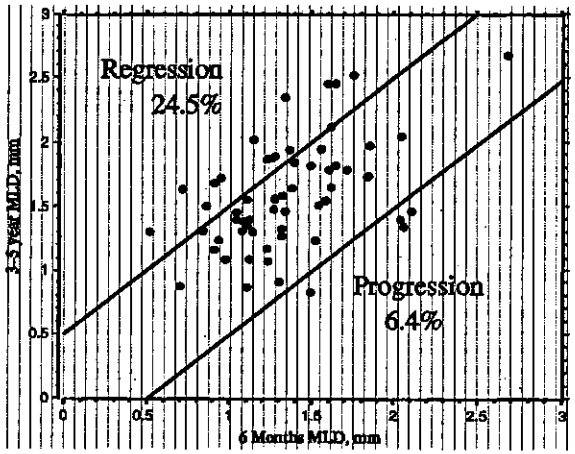

Fig 1. Lesion progression during the early (6 months) period post-balloon angioplasty, is substituted by regression up to the late (3–5 years) period.

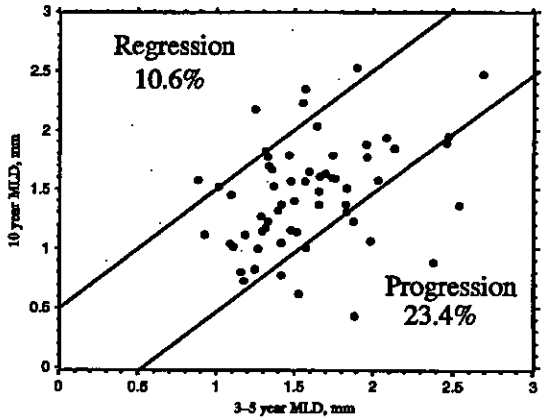

Fig 2. Progression of coronary stenosis is the prevailing feature by the long-term follow-up period (7–12 years) over the regression dominant late period (3–5 years).

luminal diameter occurred between 1 and 3 months after angioplasty, and that there was no change from 6 to 12 months! Lesion regression between 6 months and 3 years[3] or between 1 and 2 years[24] have been reported, but the actual consensus is that late lesion regression occurs between 7 months and 4.5 years after angioplasty![1]

Early restenosis is caused by the combination of neointimal thickening, consisting of smooth muscle cells and extracellular matrix, and arterial remodeling leading to vessel shrinkage. Experimental, pathological and intracoronary ultrasound studies suggest that the role of this constriction or shrinkage of the arterial in restenosis is greater than had previously been appreciated[25–30] In animals, the myointimal thickening in response to balloon injury reaches a maximum before 6 months and then regresses![13–16] This regression has been confirmed in pathological studies in humans dying at various time intervals after intracoronary metallic stent implantation; evidence of neointimal proliferation decreases with time and was difficult to find in patients who had died more than 2 years after angioplasty![31] Although the role of remodeling is not known, regression of the intimal hyperplasia after PTBA might be also the major contributor to late regression.

Other pathological studies reported that endothelial cells regenerate as the result of the healing process maturation following balloon angioplasty, during which the initially proliferated and migrated smooth muscle cells are replaced by collagen fibers or extracellular matrix![31] This process leads to luminal enlargement and result in late lesion regression, which might explain the low incidence of symptoms ascribable to the balloon-dilated site. In fact repeat angioplasty to the balloon-dilated site was required in only

1 patient up to the late (3–5 years follow-up) period in the current study.

However, while CAD progression-related ischemia did not increase from late to long-term follow-up (35.2% vs 34.3%), balloon-dilated site-related ischemia increased from 1.4% to 12.9%.

In an another pathological study of 7 years or more after balloon angioplasty demonstrated infiltration of lipid-laden macrophages mainly in the shoulder regions of the subendothelial space. After more than 10 years, thin fibrous caps heavily infiltrated by foam-cells were observed around the circumference of the lumen at balloon-dilated sites. These changes are suggestive of re-atherosclerotic process, which might be the pathogenetic mechanism of late progression or restenosis that may result in plaque vulnerability and even cause acute coronary syndromes[32] In a few lesions (n=23) analyzed at 13.3 years (range: 11.7–14.6 years) after balloon angioplasty this tendency of late progression continued further.

Inward remodeling in addition to atherosclerotic changes might have contributed to late progression in 23.4% of lesions. In a small number of lesions (10.6%), outward remodeling might have accounted for the luminal enlargement[33–36] Long-term studies using intravascular ultrasound[37,38] are needed to further elucidate the mechanism of arterial remodeling.

Study Limitations

The major limitation is the retrospective nature of the study and the potential bias by enrolling only 71 of 171 patients with successful angioplasty and serial angiographic investigation. However, there were no significant background differences between patients followed with or without angiography. Because of the retrospective nature there was a wide dispersion in the follow-up interval between late and long-term angiography.

Conclusions

The current study confirmed the lesion regression occurring up to 5 years after balloon angioplasty, but lesion progression occurred over 7 years after successful balloon angioplasty. Lesion progression is more likely to occur and be of greater magnitude in lesions with relatively little severity at 5 years. Pathologically late progression represents atherosclerotic changes and might become symptomatic beyond 7 years after the late regression phase of balloon angioplasty, but clinical events are more often caused by new non-dilated lesions at 10 or more years of observation.

Acknowledgments

The authors are indebted to Ms. Kaori Shimogama, Ms. Fusako Yoshinaga, and Ms. Makiko Kurebayashi for assistance in collecting follow-up information, and to Dr. Tadaomi-A. Miyamoto for his help with the manuscript.

References

1. Nobuyoshi M, Kimura T, Nosaka H, Mioka S, Ueno K, Yokoi H, et al. Restenosis after successful percutaneous transluminal coronary angioplasty: Serial angiographic follow-up of 229 patients. *J Am Coll Cardiol* 1988; **12:** 616–662.
2. Mabin TA, Holmes DR, Smith HC, Vlietstra RE, Reeder GS, Bresnahan JF, et al. Follow-up clinical results in patients undergoing percutaneous transluminal coronary angioplasty. *Circulation* 1985; **71:** 754–760.
3. Rosing DR, Cannon RO, Watson RM, Bonow RO, Mincemoyer R, Ewels C, et al. Three year anatomic, functional and clinical follow-up after successful percutaneous transluminal coronary angioplasty. *J Am Coll Cardiol* 1987; **9:** 1–7.
4. Talley JD, Hurst JW, King SB III, Douglas JS, Roubin GS, Gruentzig AR, et al. Clinical outcome 5 years after attempted percutaneous coronary angioplasty in 427 patients. *Circulation* 1988; **77:** 820–829.
5. Cequier A, Bonan R, Crepeau J, Cote G, Se Guise P, Joly P, et al. Restenosis and progression of coronary atherosclerosis after coronary angioplasty. *J Am Coll Cardiol* 1988; **12:** 49–55.
6. Grigg LE, Valentine PA, Manolas EG, Flower DJ, Hunt D. Long-term clinical and angiographic results following percutaneous transluminal coronary angioplasty. *Aust NZ J Med* 1988; **18:** 689–692.
7. Kamp O, Beatt KJ, De Feyter PJ, van den Brand M, Suryapranata H, Luijten HE, et al. Short-, medium-, and long-term follow-up after percutaneous transluminal coronary angioplasty for stable and unstable angina pectoris. *Am Heart J* 1989; **117:** 991–996.
8. Sharaf B, Riley RS, Drew TM, Williams DO. Late (five to eight years) clinical and angiographic assessment of patients undergoing successful percutaneous transluminal coronary angioplasty. *Am J Cardiol* 1992; **69:** 965–967.
9. Weintraub WS, Ghazzal ZMB, Douglas JS, Liberman HA, Morris DC, Cochen CL, et al. Long-term clinical follow-up in patients with angiographic restudy after successful angioplasty. *Circulation* 1993; **87:** 831–840.
10. King SB 3rd, Schlumpf M. Ten-year completed follow-up of percutaneous transluminal coronary angioplasty: The early Zurich experience. *J Am Coll Cardiol* 1993; **22:** 353–360.
11. Ormiston JA, Stewart FM, Roche AHG, Webber BJ, Whitlock RML, Webster MWI. Late regression of the dilated site after coronary angioplasty: A 5-year quantitative angiographic study. *Circulation* 1997; **96:** 468–474.
12. Guiteras-Val P, Varas-Lorenzo C, Garcia-Picart J, Marti-Claramunt V, Auge-Sanpera JM. Clinical and sequential angiographic follow-up six months and 10 years after successful transluminal coronary angioplasty. *Am J Cardiol* 1999; **83:** 868–874.
13. Inoue K, Nakamura N, Shiode N, Suyama H. Pathologic studies of late vascular responses to successful balloon angioplasty. *Circulation* 1999; **100:** I-145 (abstract).
14. Ross R, Glomset JA. The pathogenesis of atherosclerosis (first of two parts). *N Engl J Med* 1976; **295:** 369–377.
15. Stemerman MB, Ross R. Experimental atherosclerosis. I: Fibrous plaque formation in primates: An electron microscope study. *J Exp Med* 1972; **136:** 769–789.
16. Stemerman MB, Spaet TH, Pitlick F, Cintron J, Lejnieks I, Tiell ML. Intimal healing: The pattern of reendothelialization and intimal thickening. *Am J Pathol* 1977; **87:** 125–143 (abstract).
17. Fishman JA, Ryan GB, Karnovsky MJ. Endothelial regeneration in the rat carotid artery and the significance of endothelial denudation in the pathogenesis of myointimal thickening. *Lab Invest* 1975; **32:** 339–351.
18. Gruentzig AR, King SB III, Schlumpf M, Siegenthaler W. Long term follow-up after percutaneous transluminal coronary angioplasty. *N Engl J Med* 1987; **316:** 1127–1132.
19. Kaltenbach M, Kober G, Scherer D, Vallbracht C. Recurrence rate after successful coronary angioplasty. *Eur Heart J* 1985; **6:** 276–281.
20. Leimgruber PP, Roubin GS, Hollman J, Cotsonis GA, Meier B, Douglas JS, et al. Restenosis after successful coronary angioplasty in patients with single-vessel disease. *Circulation* 1986; **73:** 710–717.
21. Serruys PW, Luijten HE, Beatt KJ, Geuskins R, de Feyter PJ, van den Brand M, et al. Incidence of restenosis after successful coronary angioplasty: A time-related phenomenon. *Circulation* 1988; **77:** 361–371.
22. Hwang MH, Sibdu P, Pacold I, Johnson S, Scanlon PJ, Loeb HS. Progression of coronary artery disease after percutaneous transluminal coronary angioplasty. *Am Heart J* 1988; **115:** 297–301.
23. Hamby RI, Amin HS, Gulotta SJ, Ricciardi R. Coronary artery stenosis complicating coronary angioplasty: Report of six cases. *Am Heart J* 1987; **114:** 639–643.
24. Bruce F, Waller BF, Pinkerton CA, Foster LN. Morphorogic evidence of accerated left main coronary artery stenosis: A late complication of percutaneous balloon angioplasty of the proximal left anterior descending coronary artery. *J Am Coll Cardiol* 1987; **9:** 1019–1023.
25. Mikuriya Y, Wakayama K, Kadota M, Matsumoto Y, Tamura A, Yano S, et al. Long-term angiographic follow-up results in patients undergoing percutaneous transluminal coronary angioplasty. *Jpn Circ J* 1989; **53:** 728–734.
26. Post MJ, Borst C, Kuntz R. The relative importance of arterial remodeling compared with intimal hyperplasia in lumen renarrowing after balloon angioplasty: A study in the normal rabbit and the hypercholesterolemic Yucatan micropig. *Circulation* 1994; **89:** 2816–2821.
27. Glagov S, Weisenberg E, Zarins CK, Stankunavicrus R, Kolettis G. Compensatory enlargement of human atherosclerotic coronary arteries. *N Engl J Med* 1987; **316:** 1371–1375.
28. Glagov S. Intimal hyperplasia, vascular modeling, and the restenosis problem. *Circulation* 1994; **89:** 2888–2891.
29. Isner JM. Vascular remodeling: Honey, I think I shrunk the artery. *Circulation* 1994; **89:** 2937–2941.
30. Mintz GS, Picard AD, Kent KM, Satler LF, Popma JJ, Leon MB. Intravascular ultrasound comparison of restenotic and de novo coronary artery narrowings. *Am J Cardiol* 1994; **74:** 1278–1280.
31. Mintz GS, Popma JJ, Pichard AD, Kent KM, Satler LF, Bucher TA, et al. Differing mechanisms of late arterial responses to transcatheter therapy: A serial quantitative angiographic and intravascular ultrasound study. *J Am Coll Cardiol* 1995; **25:** 155A (abstract).
32. Katsumi I, Nobuaki N, Nobuo S, Hiromi S. Pathologic studies of late vascular responses to successful balloon angioplasty. *Circulation* 1999; **100:** I-145 (abstract).
33. Mintz GS, Pichard AD, Kent KM, Satler LF, Popma JJ, Wong CS, et al. Endovascular stents reduce restenosis by eliminating geometric arterial remodeling: A serial intravascular ultrasound study. *J Am Coll Cardiol* 1995; **25:** 35A (abstract).
34. Nobuyoshi M, Kimura T, Ohishi H, Horiuchi H, Nosaka H, Hamasaki N, et al. Restenosis after percutaneous transluminal coronary angioplasty. *J Am Coll Cardiol* 1991; **17:** 433–439.
35. Ward MR, Pasterkamp G, Yeung AC. Cornelius borst arterial remodeling: Mechanisms and clinical implications. *Circulation* 2000; **102:** 1186–1191.
36. Schoenhagen P, Ziada KM, Vince DG, Nissen SE, Tuzcu EM. Arterial remodeling and coronary artery disease: The concept of "dilated" versus "obstructive" coronary atherosclerosis. *J Am Coll Cardiol* 2001; **38:** 297–306.
37. Tamada H, Nishikawa H, Mukai S, Setsuda M, Nakamura M, Suzuki H, et al. Impact of diabetes mellitus on angiographically silent coronary atherosclerosis. *Circ J* 2003; **67:** 423–426.
38. Yamagishi M, Hosokawa H, Saito S, Kanemitsu S, Chino M, Koyanagi S, et al. Coronary disease morphology and distribution determined by quantitative angiography and intravascular ultrasound. *Circ J* 2002; **66:** 735–740.

Cardiac Functional Analysis with Multi–Detector Row CT and Segmental Reconstruction Algorithm: Comparison with Echocardiography, SPECT, and MR Imaging[1]

Evaluation of global left ventricular (LV) function, especially ejection fraction (EF), and mass is important in the treatment of various cardiac diseases. To date, cardiac functional assessment has been performed with various noninvasive modalities, such as echocardiography (1,2), nuclear medicine (3), single–detector row helical computed tomography (CT) (4), electron beam CT (5–8), and magnetic resonance (MR) imaging (9–19). Cardiac MR imaging provides excellent temporal and spatial resolution, allows image acquisition

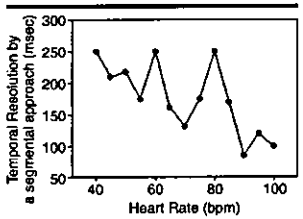

Figure 1. Graph shows temporal resolution of the multi–detector row CT system with segmental approach (rotation time, 500 msec; helical pitch, 2.0) at various heart rates. *bpm* = Beats per minute.

TABLE 1
Patient Characteristics and Final Diagnoses

Characteristics and Diagnoses	Multi–Detector Row CT and MR Imaging	Echocardiography	SPECT
Age (y)*	67 ± 10	67 ± 10	68 ± 10
Sex			
Male	28	22	17
Female	22	19	10
Heart rate (beats per minute)*	71 ± 13	71 ± 13	74 ± 13
Angina pectoris	12	9	12
Myocardial infarction	12	10	11
Valve disease	20	17	1
Other diagnoses	6	5	3
Total diagnoses	50	41	27

Note.—Unless otherwise indicated, data are numbers of patients.
* Data are mean ± standard deviation.

in any desired plane, and has a high degree of accuracy and reproducibility concerning quantitative measurements. In addition, MR imaging can be used to measure LV volume, without assumptions about LV cavity geometry. Thus, MR imaging is currently considered the reference standard in assessment of cardiac function (1,3,9–12,18,19).

In the past few years, multi–detector row CT has been increasingly used for noninvasive coronary artery imaging (20–31). In the evaluation of cardiac function, multi–detector row CT with a temporal resolution of 125–250 msec has been shown to be promising by comparing with biplanar cineventriculography (32) or MR imaging (33). However, it was indicated that reconstructed images obtained in patients with a high heart rate were of low quality because of motion artifacts; thus, manual tracing of endocardial contours had limited accuracy (32,33). A segmental reconstruction algorithm that uses data from several heartbeats has been introduced to further improve temporal resolution (34). The basic principle of segmental reconstruction is that data needed to reconstruct one image are collected retrospectively from several heartbeats by dividing into several segments. Each segment obtained in one cardiac cycle represents a shorter time period. Thus, a segmental reconstruction algorithm is considered to be effective in shortening the temporal resolution and reducing motion artifacts in patients with a high heart rate. Thus, the aim of this study was to evaluate the accuracy of cardiac functional analysis with multi–detector row CT and a segmental reconstruction algorithm over a range of heart rates.

MATERIALS AND METHODS

Phantom Studies

To evaluate artifacts of reconstruction images obtained with two retrospective electrocardiographically (ECG)-gated reconstruction methods, phantom (AZ-631N; Anzai Medical, Tokyo, Japan) studies were performed with various heart rates (every 5% of cardiac cycle, from 40 to 100 beats per minute). Method 1 involved a half reconstruction algorithm, and method 2 involved a segmental reconstruction algorithm that used data from several heartbeats. CT examinations were performed by using a multi–detector row CT scanner with eight detector rows (Aquilion Multi V1.10 JR 002 system; Toshiba, Otawara, Japan). In the scanning protocol, a collimation of 8 × 1 mm, a helical pitch of 2.0, and a rotation time of 500 msec were used. The temporal resolution with a half approach was 250 msec, while the temporal resolution with a segmental approach was further improved, depending on heart rate (Fig 1). Each helical CT scan was obtained with a tube voltage of 135 kV and a tube current of 200 mA. Image reconstruction was performed with a 1-mm increment by using both algorithms for each of these heart rates (35,36). Twenty sets of reconstructions at every 5% of the cardiac cycle, ranging from 0% to 95%, were performed in each study. One short-axis image and two long-axis cine images were reoriented from these sets of reconstruction data by using cardiac MPR software (Toshiba). The optimal end-diastolic and end-systolic phases were visually determined with these cine images.

Artifacts were evaluated on the reconstructed end-diastolic and end-systolic images of the different heart rates by two observers, each with 2 years of experience (S.K. and H.T.). The blurring artifact was scored visually with a five-point scale (0, no artifact; 1, slight artifact; 2, mild artifact; 3, moderate artifact; and 4, severe artifact). The stair-step artifact was scored with a three-point scale (0, no artifact; 1, mild artifact; and 2, severe artifact).

Human Studies

Patients referred for coronary multi–detector row CT from August 2002 to July 2003 for clinical reasons were included in this retrospective study. Among these 50 patients, MR imaging was used to assess cardiac function within 10 days before or after multi–detector row CT, during which time the condition of patients was stable. The study group consisted of 28 men (age range, 47–83 years; mean age, 67 years) and 22 women (age range, 46–84 years; mean age, 67 years). A test for the proportion with normal distribution with a 5% significance level was used to analyze the proportion of men and women, a two-sample *t* test with a 5% significance level was used to analyze the age difference between men and women, and an F test with a 5% significance level was used to analyze equality of variance between the age of men and women. No statistically significant difference was observed regarding age or sex. Mean heart rate during acquisition of CT scans ranged from 49 to 106 beats per minute (mean ± standard deviation, 71 beats per minute ± 13). A total of 20 patients had aortic and/or mitral valve disease, 12 had myocardial infarction, 12 had angina pectoris, two had infectious endocarditis, two had sarcoidosis, one had pericarditis, and one had dilated cardiomyopathy. During the same period, conventional two-dimensional echocardiography was performed in 41 patients, and ECG-gated single photon emission computed tomography (SPECT) was performed in 27. Patient characteristics and final diagnoses are shown in Table 1. Our

TABLE 2
Mean Artifact Scores in End-Diastolic and End-Systolic Phases with Half and Segmental Reconstruction Algorithms

Reconstruction Algorithm and Artifact	Heart Rate (beats/min)												
	40	45	50	55	60	65	70	75	80	85	90	95	100
	End-Diastolic Phase												
Half reconstruction algorithm													
Blurring artifact	0.0	0.0	0.0	0.0	0.5	1.0	1.5	1.0	1.0	1.0	2.0	2.5	3.0
Stair-step artifact	0.0	0.0	0.0	0.0	0.0	1.0	1.5	0.0	0.0	1.0	1.5	1.5	2.0
Segmental reconstruction algorithm													
Blurring artifact	0.0	0.0	0.0	0.0	0.5	0.0	0.0	1.0	1.0	0.0	0.0	0.0	1.0
Stair-step artifact	0.0	0.0	0.0	0.0	0.0	0.0	0.0	0.0	0.0	0.0	0.0	0.0	0.0
	End-Systolic Phase												
Half reconstruction algorithm													
Blurring artifact	0.0	0.5	1.0	1.5	1.5	2.5	2.5	3.0	3.0	3.0	3.5	4.0	4.0
Stair-step artifact	0.0	0.0	0.0	0.0	0.0	1.0	2.0	1.5	0.0	1.0	1.5	2.0	2.0
Segmental reconstruction algorithm													
Blurring artifact	0.0	0.5	1.0	0.5	1.5	1.0	1.5	1.5	3.0	2.0	0.5	1.0	2.0
Stair-step artifact	0.0	0.0	0.0	0.0	0.0	0.0	0.5	0.0	0.0	0.0	0.0	0.0	0.0

institutional review board approved this retrospective study. Informed consent was not required.

Multi-Detector Row CT and Image Interpretation

The CT scanner and scanning protocol used to examine patients were the same as those used in the phantom studies. The estimated effective radiation dose was 7.4 mSv. All patients received 100–150 mL of nonionic contrast agent through an intravenous antecubital catheter infused with a flow rate of 3.0–3.5 mL/sec without any premedication. The scanning delay was set with an automatic triggering system (SureStart; Toshiba) (37). As soon as the signal density level in the ascending aorta, which was monitored in real time, reached a predefined threshold of 150 HU, the patient was automatically instructed to maintain a breath hold; at this time, CT data and an ECG trace were obtained. Both a half and a segmental reconstruction algorithm were also applied in human studies. With the ECG trace, retrospective reconstruction was performed for acquisition of phase images starting from early systole (0% of the R-R interval) and ending at the end of diastole (95% of the R-R interval) by using 5% increasing steps; thus, 20 heart phases were obtained. One short-axis image and two long-axis cine images were created with these reconstructed data by using the same software that was used in phantom experiments. The end-diastolic and end-systolic phases were visually determined with these cine images. Short-axis images of the two phases, which covered the whole heart (10-mm section thickness), were used for functional analysis.

CT images were analyzed by an experienced observer (S.K.) without any clinical information. Manual adjustments of endocardial and epicardial borders of each short-axis image were performed. As previously described, papillary muscles were regarded as being part of the LV cavity (10,18). Subsequently, end-diastolic volume (EDV), end-systolic volume (ESV) (both were measured in milliliters), and LV mass (measured in grams) were calculated on the basis of the Simpson rule. LV mass was calculated as a product of the specific gravity of the myocardium (ie, 1.05 g/cm^3) and integrated LV myocardial area (10). Finally, the percentage of EF was calculated with EDV and ESV data (38).

Interobserver Variability of CT Measurements

Because the repeatability of multi-detector row CT measurements is relevant to the amount of agreement, interobserver variability was tested by comparing measurements obtained by two experienced observers (S.K., H.T.) at different times and without any clinical information by using data sets obtained in the first 20 patients.

MR Imaging and Image Interpretation

MR imaging was performed with a 1.5-T whole-body imager (Symphony; Siemens, Erlangen, Germany), with multiple surface coils connected to phased-array receivers. Breath-hold cine MR imaging was performed with the segmented steady-state free precession sequence (13–15). Imaging parameters were as follows: repetition time msec/echo time msec, 3.6/1.8; flip angle, 70°; seven to 15 lines per segment; matrix, 208 × 256; and field of view, 340 × 340. Cine MR images of 10–12 contiguous sections with 10-mm section thickness were obtained in the short-axis plane, covering the entire LV from the base to the apex, to acquire three-dimensional LV data (18,19).

MR images were analyzed by an observer (E.T., with 10 years of experience) without any clinical information but with the aid of commercially available software (Argus; Siemens). Image analysis was followed with manual correction of the LV border, as with multi-detector row CT. Subsequently, various functional parameters were measured with the same method.

Echocardiography and Image Interpretation

For two-dimensional echocardiography, patients underwent imaging in the left lateral decubitus position by using a commercially available system (Sonos 5500; Hewlett-Packard, Palo Alto, Calif). Images were obtained by an observer (M.O., with 8 years of experience) using a 3.5-MHz transducer in the parasternal (long- and short-axis) and apical (two- and four-chamber views) planes and were saved in cine loop format. EF was calculated by the same observer, who was blinded to other information obtained with two- and four-chamber images, and who used the previously validated biplanar Simpson rule (1,2,38–41).

ECG-gated SPECT and Image Interpretation

Each patient underwent exercise thallium 201 (^{201}Tl) SPECT, as described previously (18,42). At the peak exercise level, approximately 74 MBq of ^{201}Tl was injected intravenously. Approximately 10 minutes after the termination of exercise, initial SPECT was performed. Approximately 3–4 hours after termination of the initial examination, an additional 37 MBq of ^{201}Tl was injected, and reinjection SPECT was performed. ECG-gated SPECT images were obtained with a dual-head gamma camera (Millennium; GE Medical Systems, Milwaukee, Wis) equipped with low-energy thin section collimation (30 projections over 180°, eight frames per cardiac cycle, 60 seconds per projection). Two energy windows were used (ie, 30% windows centered on the 70- and 167-keV peaks). ECG-gated perfusion SPECT images were prefiltered with Butterworth filter (order, five; voxel size, 7.2 mm; cut-off frequency, 0.40 cycles per pixel) (18). A zoom factor of 1.28 was used. Data were reconstructed by using a filtered back-projection technique with no attenuation or scatter correction. The EF was automatically calculated with reinjection SPECT images by using the Germano algorithm (3,18,19,43).

Statistical Analysis

Data are expressed as mean ± standard deviation. Evaluation of agreement between artifact scores of the phantom was performed by using κ statistics. Systemic error and the degree of agreement of global functional parameters obtained with multi-detector row CT and MR imaging were assessed according to the method described by Bland and Altman (44). Systemic error and the degree of agreement of EF, as calculated with echocardiography and MR imaging data and ECG-gated SPECT and MR imaging data, respectively, were assessed with the same method. The degree of agreement between the two methods was determined as the mean difference (bias), standard deviation of the differences, limits of agreement (mean ± 2 standard deviations), standard error of the mean difference, and 95% confidence interval of the mean difference. A one-sample *t* test at the 5% significance level was used to determine whether the resulting difference from zero, as an under- or overestimation with multi-detector row CT, was significant. F ratios were used to describe the equality of the standard deviation of difference of EF values obtained with multi-detector row CT with a segmental reconstruction algorithm and MR imaging to EF values obtained with echocardiography and MR imaging and EF values obtained with ECG-gated SPECT and MR imaging.

In a second analysis, linear regression analysis was used to compare the functional values obtained with multi-detector row CT, echocardiography, and ECG-gated SPECT with MR imaging. F ratios were used to describe the equality of standard error of estimates of EF between the correlation of multi-detector row CT with a segmental reconstruction algorithm and MR imaging, between echocardiography and MR imaging, and between ECG-gated SPECT and MR imaging. A *P* value of less than .05 was considered to indicate statistical significance.

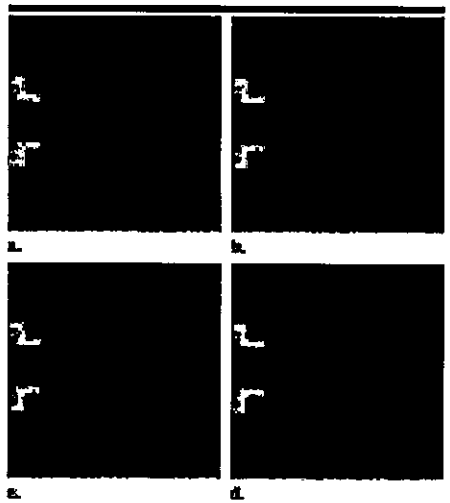

Figure 2. End-diastolic and end-systolic vertical long-axis CT scans of a phantom were reconstructed with half and segmental reconstruction algorithms at a heart rate of 95 beats per minute. (a) End-diastolic and (b) end-systolic vertical long-axis CT scans obtained with half approach. (c) End-diastolic and (d) end-systolic vertical long-axis CT scans obtained with segmental approach. Severe artifacts were observed with a half approach, especially in the end-systolic phase, while no severe artifacts were observed with a segmental approach. Artifacts of reconstructed images obtained with a half approach were so severe that determination of the myocardial outline was difficult.

RESULTS

Phantom Studies

The results of phantom studies are shown in Table 2. The κ value for evaluation of agreement between the blurring artifact scores was 0.58, while that between the stair-step artifacts was 0.73. Various artifacts were observed in patients with higher heart rates (≥65 beats per minute) who were evaluated with a half reconstruction algorithm; no substantial artifacts were found in patients evaluated with a segmental reconstruction algorithm, except in those with a heart rate of 80 beats per minute. In patients with higher heart rates (≥65 beats per minute), artifacts of reconstructed images obtained with a half reconstruction algorithm were generally so severe that determination of the myocardial outline was difficult (Fig 2).

Human Studies

No substantial motion artifact was observed, even in patients with a high heart

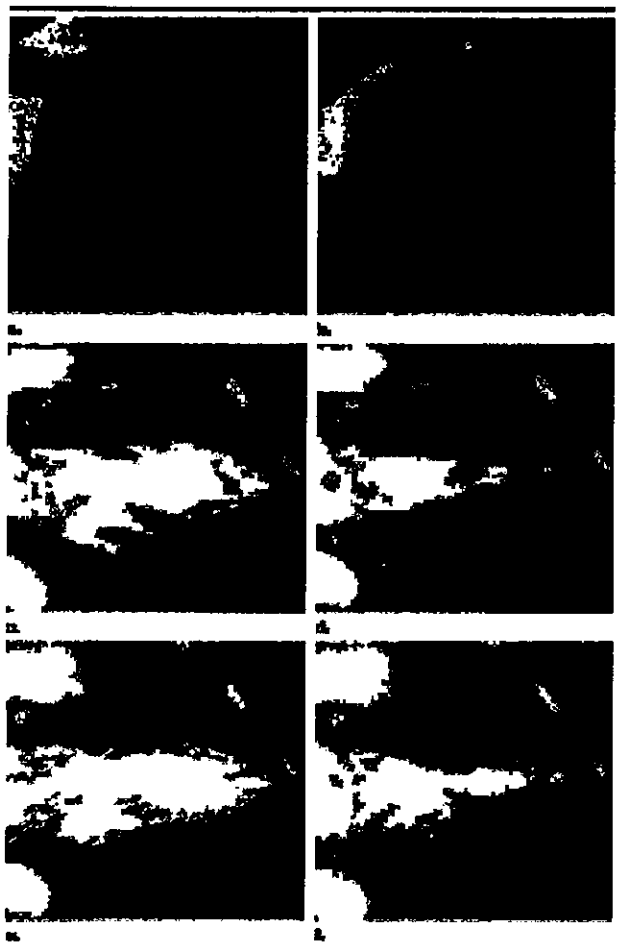

Figure 3. End-diastolic and end-systolic short-axis and vertical long-axis CT scans were reconstructed with a segmental reconstruction algorithm in a patient with a heart rate of 98 beats per minute. (a) Typical end-diastolic and (b) corresponding end-systolic short-axis CT scans. (c) End-diastolic and (d) end-systolic vertical long-axis CT scans. Epicardial (black line in a and b) and endocardial (white line in a and b) tracings exclude epicardial fat and include papillary muscles within ventricular cavity. No severe artifact was found on these scans. End-diastolic and end-systolic vertical long-axis scans were also reconstructed with a half reconstruction algorithm in the same patient. (e) End-diastolic and (f) end-systolic vertical long-axis CT scans. Artifacts of reconstructed images obtained with a half reconstruction algorithm were more severe than those obtained with a segmental approach. Of note, the end systolic size of the LV cavity appeared larger on scans obtained with a half approach than on scans obtained with a segmental approach. Angina pectoris was diagnosed in this patient.

rate, when a segmental reconstruction approach was used. On the other hand, artifacts were generally more severe on reconstructed images obtained with a half approach than on images obtained with a segmental approach if the heart rate was higher (Fig 3).

A summary of data obtained with multi–detector row CT, echocardiography, ECG-gated SPECT, and MR imaging is presented in Tables 3–5. Results of the Bland-Altman analysis are shown in Tables 6–8 and Figures 4–6. Bland-Altman analysis revealed no significant degree of directional measurement bias when data obtained with multi–detector row CT and segmental reconstruction algorithm were compared with data obtained with MR imaging ($n = 50$). No significant difference of the mean difference from 0 was found for any parameter ($n = 50$). On the other hand, significant overestimation of ESV ($P < .01$) and underestimation of EF ($P < .001$) were observed with a half approach ($n = 50$). In terms of EF, the standard deviation of difference between multi–detector row CT with a segmental reconstruction algorithm and MR imaging was significantly less than that between echocardiography and MR imaging ($n = 41$, $P < .001$) or that between ECG-gated SPECT and MR imaging ($n = 27$, $P < .001$).

The results of linear regression analysis are shown in Tables 9–11. The data (EF, EDV, ESV, and LV mass) obtained with multi–detector row CT were closely correlated with the data obtained with MR imaging ($n = 50$). In terms of EF, the standard error of the estimate between multi–detector row CT with a segmental reconstruction algorithm and MR imaging was significantly smaller than that between echocardiography and MR imaging ($n = 41$, $P < .001$) or that between ECG-gated SPECT and MR imaging ($n = 27$, $P < .001$).

Interobserver Variability of CT Measurements

An interobserver variability of 8.6% for EF, 7.3% for EDV, 9.6% for ESV, and 10.4% for LV mass was found with the half reconstruction algorithm. On the other hand, an interobserver variability of 5.7% for EF, 6.9% for EDV, 7.0% for ESV, and 9.3% for LV mass was found with the segmental reconstruction algorithm. These results revealed small interobserver variability among the multi–detector row CT measurements.

DISCUSSION

Our results demonstrate that the LV values, including EF, EDV, ESV, and LV mass, obtained with multi–detector row CT and a segmental reconstruction algorithm correlated and agreed with those obtained with MR imaging over a wide range of heart rates. Moreover, functional analysis with multi–detector row CT and a segmental reconstruction algorithm was more accurate than analysis performed with two-dimensional echocardiography or ECG-gated SPECT.

Among the many factors that may affect the accuracy of LV functional measurements with multi–detector row CT, the main limitation is the fact that temporal resolution is worse with multi–detector row CT than with MR imaging (ap-

TABLE 3
LV Measurements with Multi–Detector Row CT and MR Imaging in 50 Patients

Modality and Algorithm	LV EF (%)	EDV (mL)	ESV (mL)	LV Mass (g)
Multi–detector row CT				
Half reconstruction algorithm	46.5 ± 14.4 (12–70)	153.5 ± 59.4 (81–342)	86.2 ± 53.7 (31–263)	142.2 ± 61.7 (60–347)
Segmental reconstruction algorithm	50.1 ± 16.2 (12–76)	153.7 ± 59.5 (85–322)	81.7 ± 55.8 (27–262)	141.1 ± 56.9 (76–326)
MR imaging	51.3 ± 16.1 (12–78)	154.0 ± 64.3 (63–334)	80.6 ± 57.8 (25–257)	138.6 ± 53.9 (67–316)

Note.—Data are mean ± standard deviation. Data in parentheses are the range.

TABLE 4
LV EF in 41 Patients

Modality	LV EF (%)
Echocardiography	54.6 ± 16.7 (15–86)
Multi–detector row CT with segmental reconstruction algorithm	50.7 ± 16.0 (12–76)
MR imaging	51.8 ± 15.9 (12–78)

Note.—Data are mean ± standard deviation. Data in parentheses are the range.

TABLE 5
LV EF in 27 Patients

Modality	LV EF (%)
ECG-gated SPECT	39.6 ± 17.5 (12–74)
Multi–detector row CT	43.1 ± 15.9 (12–75)
MR imaging	43.3 ± 15.0 (12–67)

Note.—Data are mean ± standard deviation. Data in parentheses are the range.

TABLE 6
Multi–Detector Row CT and MR Imaging in 50 Patients

Algorithm and Statistics	LV EF (%)	EDV (mL)	ESV (mL)	LV Mass (g)
Half reconstruction algorithm				
Bias*	−4.7 ± 6.0	−0.49 ± 18.2	5.5 ± 12.4	3.6 ± 19.9
Limits of agreement†	12.0	36.3	24.8	39.8
95% CI	1.7	5.0	3.4	5.5
Standard error of the mean difference	0.8	2.6	1.8	2.8
Regression line	y = −0.11 × +0.8	y = −0.08 × +12.1	y = 0.075 × +11.8	y = 0.14 × −16.0
Segmental reconstruction algorithm				
Bias*	−1.2 ± 4.6	−0.35 ± 15.2	1.1 ± 8.6	2.5 ± 15.0
Limits of agreement†	9.3	30.5	17.3	30.0
95% CI	1.3	4.2	2.4	4.2
Standard error of the mean difference	0.7	2.2	1.2	2.1
Regression line	y = 0.005 × −1.5	y = −0.079 × +11.7	y = −0.036 × +4.0	y = 0.057 × −5.4

Note.—Bland-Altman analysis revealed significant overestimation of ESV ($P < .01$) and underestimation of EF ($P < .001$) in a half approach compared with MR imaging. No significant degree of directional measurement bias was observed in any of the comparisons of multi–detector row CT with a segmental reconstruction algorithm and MR imaging data. No significant difference of the mean difference from 0 was found for any parameter with a segmental approach. CI = confidence interval.
* Data are mean ± standard deviation.
† Two standard deviations.

TABLE 7
EF Difference between Multi–Detector Row CT and MR Imaging and between Echocardiography and MR Imaging

Statistics	Multi–Detector Row CT and MR Imaging (%)	Echocardiography and MR Imaging (%)
Bias*	−1.1 ± 4.1	2.6 ± 9.3
Limits of agreement†	8.2	18.6
95% CI	1.3	2.9
Standard error of the mean difference	0.6	1.5
Regression line	y = 0.007 × −1.5	y = 0.41 × +0.38

Note.—The standard deviation of difference between multi–detector row CT and MR imaging was significantly less than that between echocardiography and MR imaging ($P < .001$). CI = confidence interval.
* Data are mean ± standard deviation.
† Two standard deviations.

TABLE 8
EF Difference between Multi–Detector Row CT and MR Imaging and between ECG-gated SPECT and MR Imaging

Statistics	Multi–Detector Row CT and MR Imaging (%)	ECG-gated SPECT and MR Imaging (%)
Bias*	−0.2 ± 3.7	−3.6 ± 9.9
Limits of agreement†	7.4	19.8
95% CI	1.4	3.7
Standard error of the mean difference	0.7	1.9
Regression line	y = 0.062 × −2.8	y = 0.17 × −10.8

Note.—The standard deviation of difference between multi–detector row CT and MR imaging was significantly less than that between ECG-gated SPECT and MR imaging ($P < .001$). CI = confidence interval.
* Data are mean ± standard deviation.
† Two standard deviations.

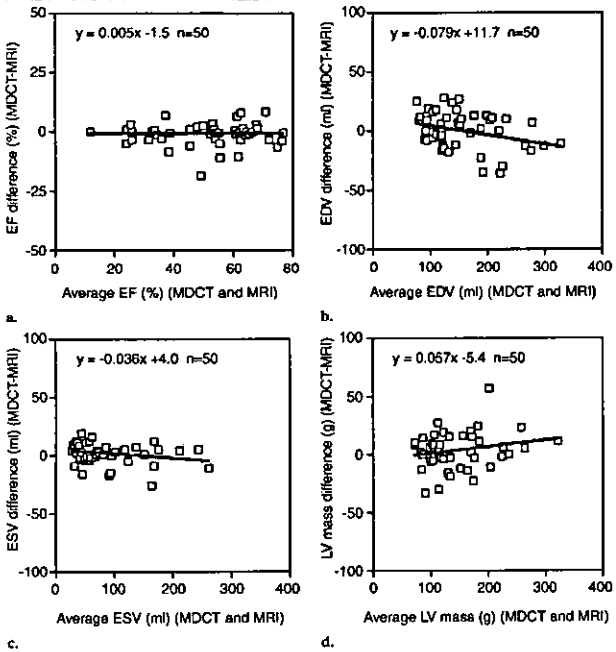

Figure 4. Graphs created with Bland-Altman analysis of (a) LV EF, (b) EDV, (c) ESV, and (d) LV mass, as measured with multi–detector row CT *(MDCT)* with a segmental reconstruction algorithm and MR imaging in 50 patients. Graphs show close agreement between multi–detector row CT and MR imaging. The slopes of the regression lines were not significantly different from 0. No significant differences of the mean difference from 0 were found.

proximately 50 msec). A single helical CT study with a temporal resolution of 400 msec (4) and recent multi–detector row CT studies with a temporal resolution of 125–250 msec performed with a half or biphasic reconstruction algorithm showed close correlation with cineventriculography (32) and MR imaging (33) studies, in terms of EF. Because of the limited temporal resolution, however, systolic images, especially those obtained in patients with a higher heart rate, were shown to be of lower quality (32,33). Additionally, ESV was overestimated, while EDV was not significantly different (4). As a result, underestimation of EF was noted in these studies. In our study, artifacts of reconstructed images obtained with a half approach (temporal resolution of 250 msec) were generally severe if the heart rate was high. In addition, overestimation of ESV and underestimation of EF were observed when a half approach was applied. Juergens et al (32) suggested that data reconstruction algorithms that use segmental data from several heartbeats will likely allow optimization of the analysis of cardiac function with multi–detector row CT. In fact, our phantom experiments demonstrated that a segmental reconstruction algorithm, in which several sets of heartbeat data were used, was more appropriate than a half reconstruction algorithm in terms of reducing motion artifacts, especially in patients with high heart rates.

In the current human studies, no substantial motion artifact was observed, even in patients with a high heart rate, when a segmental reconstruction approach was used. In addition, the various LV functional values obtained with multi–detector row CT and a segmental reconstruction method were shown to correlate and agree with those obtained with MR imaging, which was in agreement with the findings of the preliminary study of Halliburton et al (34). Of note, the standard deviation of EF difference between multi–detector row CT with a segmental approach and MR imaging was significantly less than that between echocardiography and MR imaging or ECG-gated SPECT and MR imaging. Thus, functional analysis with multi–detector row CT and a segmental approach was considered more accurate than functional analysis with two-dimensional echocardiography or ECG-gated SPECT. Previous reports (1,2) suggest that two-dimensional echocardiography is a poor modality to use in the assessment of LV volume and function when ventricular geometry is not uniform. ECG-gated SPECT is also limited when large LV perfusion defects exist (45) or the heart is small (46).

In general, a segmental reconstruction algorithm is effective in shortening the temporal resolution and reducing motion artifacts. At a certain heart rate, however, temporal resolution is not improved, even with a segmental reconstruction approach. For example, in patients with a heart rate of 80 beats per minute, a temporal resolution of 250 msec is not improved—even with a segmental reconstruction algorithm—which results in increased artifacts in our phantom study. Thus, the functional assessment of certain heart rates may still be less than ideal. A more rapid rotation time (approximately 0.4 seconds per rotation) has been attained with multi–detector row CT (23,34), which will make it possible to shorten and stabilize the temporal resolution with a segmental approach. As a result, functional assessment with multi–detector row CT will be further improved.

Our results reveal good repeatability among multi–detector row CT measurements, especially with a segmental approach, which indicates that determination of LV border with multi–detector row CT and a segmental approach is accurate and reliable. In fact, we did not encounter substantial difficulties due to motion artifacts when determining the LV border, even in patients with a high heart rate. Although there was no significant difference between the mean value of various functional parameters as determined with multi–detector row CT and MR imaging, the Bland-Altman plot reveals wide limits of agreement. In addition, temporal resolution of a segmental reconstruction algorithm is dependent on heart rate, which is not the case with MR imaging. These findings suggest that LV functional measurements obtained with multi–detector row CT and MR imaging may not be interchangeable.

Recent reports show that the use of a β-blocker is effective in lowering heart rates and reducing motion artifacts (31). According to the literature, however, a β-blocker decreases heart rates by an average of only 8 beats per minute (31). In addition, Vogl et al (22) reported that use of a β-blocker did not produce any effect in some patients. Thus, use of a β-blocker is not always effective in the reduction of motion artifacts. In addition, premedication is troublesome in clinical settings, because careful observation and a prolonged stay are required (23); therefore, β-blockers were not routinely used in our institution. Instead, a segmental reconstruction algorithm has been used to improve temporal resolution when the heart rate is high. A segmental approach may not be useful in the precise assessment of coronary arteries, however, especially when the R-R interval is irregular. At present, there is no definitive solution when the heart rate is high and irregular (23). In addition, the use of a β-blocker changes the LV function (47). Thus, functional parameters, with the exception of LV mass, can be unreliable after such premedication. To obtain functional data as added information, use of a β-blocker is unacceptable.

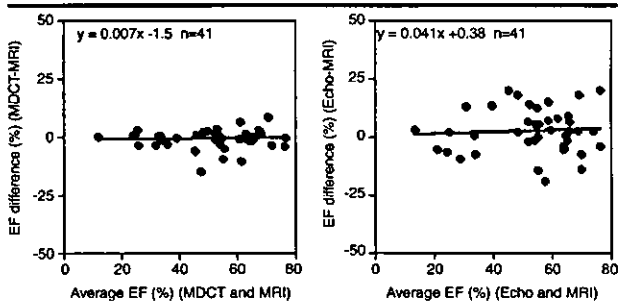

Figure 5. Graphs created with Bland-Altman analysis of LV EF in 41 patients, as measured with (a) multi–detector row CT *(MDCT)* with a segmental reconstruction algorithm and MR imaging or (b) echocardiography and MR imaging. Graphs clearly show that the dispersion between multi–detector row CT and MR imaging was significantly less than that between echocardiography and MR imaging ($P < .001$).

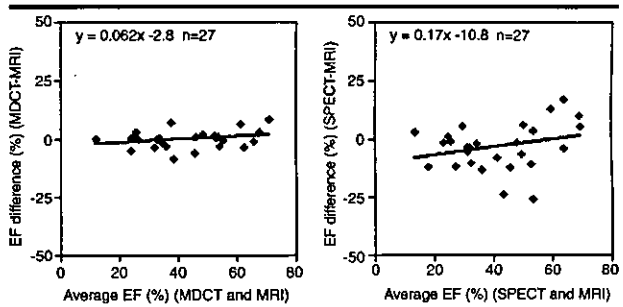

Figure 6. Graphs created with Bland-Altman analysis of LV EF in 27 patients, as measured with (a) multi–detector row CT *(MDCT)* with a segmental reconstruction algorithm and MR imaging or (b) ECG-gated SPECT and MR imaging. Graphs clearly show that the dispersion between multi–detector row CT and MR imaging was significantly less than that between ECG-gated SPECT and MR imaging ($P < .001$).

Radiation dose reduction is clinically important. A large helical pitch, reduced tube current, increased number of detector rows, and faster rotation time can be used to reduce the radiation dose. For example, a larger helical pitch will lead to reduced radiation exposure. When the helical pitch is greater, however, the temporal resolution with a segmental approach becomes worse, which may decrease data fidelity not only for multi–detector row CT coronary information but also for functional analysis. Reduced tube current would serve to directly reduce radiation exposure. Reduced tube current will, however, cause increased image noise. For these reasons, a larger helical pitch or reduced tube current should be avoided (30). Recently, a multi–detector row CT scanner equipped with more detector rows and a faster rotation time has been introduced, resulting in reduction of the radiation dose. In addition, lowering the tube current during unneeded phases of the cycle (48) is effective for radiation dose reduction.

TABLE 9
Linear Regression Analysis between Multi–Detector Row CT and MR Imaging in 50 Patients

Algorithm and Statistics	LV EF	EDV	ESV	LV Mass
Half reconstruction algorithm				
Correlation coefficient	0.93	0.96	0.98	0.95
Standard error of estimates	5.4	17.0	11.4	19.7
Regression line	y = 0.83x + 3.8	y = 0.89x + 17.1	y = 0.91x + 13.0	y = 1.09x − 8.7
Segmental reconstruction algorithm				
Correlation coefficient	0.96	0.97	0.99	0.96
Standard error of estimates	4.4	14.0	8.4	15.4
Regression line	y = 0.97x + 0.5	y = 0.90x + 15.6	y = 0.96x + 4.9	y = 1.01x − 1.1

Note.—Values obtained with multi–detector row CT were closely correlated with those obtained with MR imaging.

TABLE 10
Linear Regression Analysis for EF between Echocardiography and MR Imaging and between Multi–Detector Row CT with a Segmental Reconstruction Algorithm and MR Imaging in 41 Patients

Statistics	Multi–Detector Row CT and MR Imaging	Echocardiography and MR Imaging
Correlation coefficient	0.95	0.84
Standard error of estimates	5.0	9.2
Regression line	y = 0.92x + 2.4	y = 0.84x + 10.5

Note.—Standard error of estimates between multi–detector row CT and MR imaging was significantly less than that between echocardiography and MR imaging ($P < .001$).

TABLE 11
Linear Regression Analysis for EF between ECG-Gated SPECT and MR Imaging and between Multi–Detector Row CT with a Segmental Reconstruction Algorithm and MR Imaging in 27 Patients

Statistics	Multi–Detector Row CT and MR Imaging	ECG-gated SPECT and MR Imaging
Correlation coefficient	0.97	0.83
Standard error of estimates	3.6	8.8
Regression line	y = 1.04x − 1.7	y = 0.97x − 2.2

Note.—Standard error of estimates between multi–detector row CT and MR imaging was significantly smaller than that between ECG-gated SPECT and MR imaging ($P < .001$).

Unfortunately, this strategy may influence the reliability of functional analysis.

The use of multi–detector row CT solely in the assessment of cardiac function does not appear reasonable because of the radiation exposure. It is important, however, that a functional analysis can be conducted by using data obtained with noninvasive coronary imaging without an increase in cost, volume of contrast agent administered, or radiation dose. We believe that multi–detector row CT will be useful in the comprehensive evaluation of coronary arteries and resting LV function.

A limitation of the F test may be the possible violation of the independence assumption, since the variances are about measures taken on the same subject. The critical F values were used for comparison purposes, and statistical significance was not necessarily implied.

In conclusion, the various LV functional parameters of multi–detector row CT with a segmental reconstruction algorithm obtained by using data from several heartbeats correlated and agreed with those obtained with MR imaging. Moreover, the functional analysis with multi–detector row CT with a segmental reconstruction algorithm was more accurate than that with two-dimensional echocardiography or ECG-gated SPECT.

References

1. Buck T, Hunold P, Wentz KU, Tkalec W, Nesser HJ, Erbel R. Tomographic three-dimensional echocardiographic determination of chamber size and systolic function in patients with left ventricular aneurysm. Circulation 1997; 96:4286–4297.
2. Qin JX, Jones M, Shiota T, et al. Validation of real-time three-dimensional echocardiography for quantifying left ventricular volumes in the presence of a left ventricular aneurysm: in vitro and in vivo studies. J Am Coll Cardiol 2000; 36:900–907.
3. Bavelaar-Croon CD, Kayser HW, van der Wall EE, et al. Left ventricular function: correlation of quantitative gated SPECT and MR imaging over a wide range of values. Radiology 2000; 217:572–575.
4. Mochizuki T, Murase K, Higashino H, et al. Two- and three-dimensional CT ventriculography: a new application of helical CT. AJR Am J Roentgenol 2000; 174: 203–208.
5. Lessick J, Sideman S, Azhari H, Marcus M, Grenadier E, Beyar R. Regional three-dimensional geometry and function of left ventricles with fibrous aneurysms: a cine-computed tomography study. Circulation 1991; 84:1072–1086.
6. Lipton MJ, Higgins CB, Farmer D, Boyd DP. Cardiac imaging with a high-speed cine-CT scanner: preliminary results. Radiology 1984; 152:579–582.
7. Lipton MJ, Farmer DW, Killebrew EJ, et al. Regional myocardial dysfunction: evaluation of patients with prior myocardial infarction with fast CT. Radiology 1985; 157:735–740.
8. Rees MR, Feiring AJ, Rumberger JA, MacMillan RM, Clark DL. Heart evaluation by cine CT: use of two new oblique views. Radiology 1986; 159:804–806.
9. Higgins CB. Which standard has the gold? (editorial). J Am Coll Cardiol 1992; 19:1608–1609.
10. Pattynama PM, Lamb HJ, van der Velde EA, van der Wall EE, de Roos A. Left ventricular measurements with cine and spin-echo MR imaging: a study of reproducibility with variance component analysis. Radiology 1993; 187:261–268.
11. Bellenger NG, Burgess MI, Ray SG, et al. Comparison of left ventricular ejection fraction and volumes in heart failure by echocardiography, radionuclide ventricography, cardiovascular magnetic resonance; are they interchangeable? Eur Heart J 2000; 21:1387–1396.
12. de Roos A, Kunz P, Lamb H, et al. Magnetic resonance imaging of ischemic heart disease: why cardiac magnetic resonance imaging will play a significant role in the management of patients with coronary artery disease. J Comput Assist Tomogr 1999; 23(suppl 1):S135–S141.
13. Barkhausen J, Ruehm SG, Goyen M, et al. MR evaluation of ventricular function: true fast imaging with steady-state precession versus fast low-angle shot cine MR imaging: feasibility study. Radiology 2001; 219:264–269.
14. Carr JC, Simonetti O, Bundy J, Li D, Pereles S, Finn JP. Cine MR angiography of the heart with segmented true fast imaging with steady-state precession. Radiology 2001; 219:828–834.
15. Miller S, Simonetti OP, Carr J, Kramer U, Finn JP. MR imaging of the heart with cine true fast imaging with steady-state precession: influence of spatial and temporal resolutions on left ventricular functional parameters. Radiology 2002; 223: 263–269.
16. Heusch A, Koch JA, Krogmann ON, Korbmacher B, Bourgeois M. Volumetric analysis of the right and left ventricle in a porcine heart model: comparison of three-dimensional echocardiography, magnetic resonance imaging and angiography. Eur J Ultrasound 1999; 9:245–255.
17. Lorenz CH, Walker ES, Morgan VL, Klein SS, Graham TP Jr. Normal human right and left ventricular mass, systolic function, and gender differences by cine magnetic resonance imaging. J Cardiovasc Magn Reson 1999; 1:7–21.
18. Tadamura E, Kudoh T, Motooka M, et al. Assessment of regional and global left ventricular function by reinjection Tl-201 SPECT and rest Tc-99m sestamibi ECG-gated SPECT. J Am Coll Cardiol 1999; 33: 991–997.
19. Tadamura E, Kudoh T, Motooka M, et al. Use of technetium-99m sestamibi ECG-gated single-photon emission tomography for the evaluation of left ventricular function following coronary artery bypass graft: comparison with three-dimensional magnetic resonance imaging. Eur J Nucl Med 1999; 26:705–712.
20. Nieman K, Oudkerk M, Rensing BJ, et al. Coronary angiography with multi-slice computed tomography. Lancet 2001; 357:599–603.
21. Achenbach S, Giesler T, Ropers D, et al. Detection of coronary artery stenoses by contrast-enhanced, retrospectively electrocardiographically-gated, multislice spiral computed tomography. Circulation 2001; 103:2535–2538.
22. Vogl TJ, Abolmaali ND, Diebold T, et al. Techniques for the detection of coronary atherosclerosis: multi-detector row CT coronary angiography. Radiology 2002; 223:212–220.
23. Nieman K, Cademartiri F, Lemos PA, Raaijmakers R, Pattynama PM, Feyter PJ. Reliable noninvasive coronary angiography with fast submillimeter multislice spiral computed tomography. Circulation 2002; 106:2051–2054.
24. Schroeder S, Kopp AF, Baumbach A, et al. Noninvasive detection and evaluation of atherosclerotic coronary plaques with multislice computed tomography. J Am Coll Cardiol 2001; 37:1430–1435.
25. Horiguchi J, Nakanishi T, Ito K. Quantification of coronary artery calcium using multidetector CT and a retrospective ECG-gating reconstruction algorism. AJR Am J Roentgenol 2001; 177:1429–1435.
26. White RD, Setser RM. Integrated approach to evaluating coronary artery disease and ischemic heart disease. Am J Cardiol 2002; 90:49L–55L.
27. Hong C, Becker CR, Schoepf UJ, Ohnesorge B, Bruening R, Reiser MF. Coronary artery calcium: absolute quantification in nonenhanced and contrast-enhanced multi–detector row CT studies. Radiology 2002; 223:474–480.
28. Willmann JK, Weishaupt D, Lachat M, et al. Electrocardiographically gated multi–detector row CT for assessment of valvular morphology calcification in aortic stenosis. Radiology 2002; 225:120–128.
29. Hong C, Becker CR, Huber A, et al. ECG-gated reconstructed multi–detector row CT coronary angiography: effect of varying trigger delay on imaging quality. Radiology 2001; 220:712–717.
30. Kopp AF, Schroeder S, Kuettner A, et al. Coronary arteries: retrospectively ECG-gated multi-detector row CT angiography with selective optimization of the image reconstruction window. Radiology 2001; 221:683–688.
31. Ropers D, Baum U, Pohle K, et al. Detection of coronary artery stenoses with thin-slice multi-detector row spiral computed tomography and multiplanar reconstruction. Circulation 2003; 107:664–666.
32. Juergens KU, Grude M, Fallenberg EM, et al. Using ECG-gated multidetector CT to evaluate global left ventricular myocardial function in patients with coronary artery disease. AJR Am J Roentgenol 2002; 179:1545–1550.
33. Juergens KU, Grude M, Maintz D, et al. Multi–detector row CT of left ventricular function with dedicated analysis software versus MR imaging: initial experience. Radiology 2004; 230:403–410.
34. Halliburton SS, Boese JM, Flohr TG, Lieber ML, Kuzmiak SA, White RD. Improved volumetric analysis of the left ventricle using cardiac multislice computed tomography (MSCT) with high temporal resolution image reconstruction (abstr). Radiology 2002; 225(P):389.
35. Ota T, Taguchi K. A navigation tool to assist optimal scan protocol of electrocardiogram (ECG)-gated retrospective reconstruction for multislice helical CT (abstr). Radiology 2001; 221(P):690.
36. Flohr T, Ohnesorge B. Heart rate adaptive optimization of spatial and temporal resolution for electrocardiogram-gated multislice spiral CT of the heart. J Comput Assist Tomogr 2001; 25:907–923.
37. Takase K, Sawamura Y, Igarashi K, et al. Demonstration of the artery of Adamkiewicz at multidetector row helical CT. Radiology 2002; 223:39–45.
38. Dirksen MS, Bax JJ, de Roos A, et al. Usefulness of dynamic multislice computed tomography of left ventricular function in unstable angina pectoris and comparison with echocardiography. Am J Cardiol 2002; 90:1157–1160.
39. Schiller NB, Acquatella H, Ports TA, et al. Left ventricular volume from paired biplane two-dimensional echocardiography. Circulation 1979; 60:547–555.
40. Gordon EP, Schnittger I, Fitzgerald PJ, Williams P, Popp RL. Reproducibility of left ventricular volumes by two-dimensional echocardiography. J Am Coll Cardiol 1983; 2:506–513.
41. Otterstad JE, Froeland G, St John SM, Holme I. Accuracy and reproducibility of biplane two-dimensional echocardiographic measurements of left ventricular dimensions and function. Eur Heart J 1997; 18:507–513.
42. Takahashi N, Tamaki N, Tadamura E, et al. Combined assessment of regional perfusion and wall motion in patients with coronary artery disease with technetium-99m tetrofosmin. J Nucl Cardiol 1994; 1:29–38.
43. Germano G, Kiat H, Kavanagh PB, et al. Automatic quantification of ejection fraction from gated myocardial perfusion SPECT. J Nucl Med 1995; 36:2138–2147.
44. Bland JM, Altman DG. Statistical methods for assessing agreement between two methods of clinical measurement. Lancet 1986; 1:307–310.
45. Manrique A, Faraggi M, Vera P, et al. Tl-201 and Tc-99m MIBI gated SPECT in patients with large perfusion defects and left ventricular dysfunction: comparison with equilibrium radionuclide angiography. J Nucl Med 1999; 40:805–809.
46. Mazzanti M, Germano G, Kiat H, et al. Identification of severe and extensive coronary artery disease by automatic measurement of transient ischemic dilation of the left ventricle in dual-isotope myocardial perfusion SPECT. J Am Coll Cardiol 1996; 27:1612–1620.
47. Ooi H, Colucci WS. Pharmacological treatment of heart failure. In: Hardmann JG, Limbird LE, Gilman AG, eds. The pharmacological basis of therapeutics. 10th ed. New York, NY: McGraw-Hill, 2001; 913–916.
48. Jakobs TF, Becker CR, Ohnesorge B, et al. Multislice helical CT of the heart with retrospective ECG gating: reduction of radiation exposure by ECG-controlled tube current modulation. Eur Radiol 2002; 12: 1081–1086.

Available online at www.sciencedirect.com
SCIENCE DIRECT
ELSEVIER
Biochemical and Biophysical Research Communications 331 (2005) 1295–1300
BBRC
www.elsevier.com/locate/ybbrc

CXCL16 is a novel angiogenic factor for human umbilical vein endothelial cells

Xin Zhuge [a,1], Toshinori Murayama [a,1], Hidenori Arai [b,*], Ryoko Yamauchi [b], Makoto Tanaka [b], Takeshi Shimaoka [d], Shin Yonehara [d], Noriaki Kume [c], Masayuki Yokode [a], Toru Kita [c]

[a] *Department of Clinical Innovative Medicine, Kyoto University Graduate School of Medicine, 54 Kawahara-cho, Shogoin, Sakyo-ku, Kyoto 606-8507, Japan*
[b] *Department of Geriatric Medicine, Kyoto University Graduate School of Medicine, 54 Kawahara-cho, Shogoin, Sakyo-ku, Kyoto 606-8507, Japan*
[c] *Department of Cardiovascular Medicine, Kyoto University Graduate School of Medicine, 54 Kawahara-cho, Shogoin, Sakyo-ku, Kyoto 606-8507, Japan*
[d] *Institute for Virus Research, Kyoto University Graduate School of Medicine, 54 Kawahara-cho, Shogoin, Sakyo-ku, Kyoto 606-8507, Japan*

Received 23 March 2005
Available online 6 April 2005

Abstract

CXCL16 is a unique chemokine with characteristics as a receptor for phosphatidylserine and oxidized low density lipoproteins in macrophages, and is involved in the accumulation of cellular cholesterol during atherosclerotic lesion development. In this study, we report a new function of CXCL16 as a novel angiogenic factor in human umbilical vein endothelial cells (HUVEC). CXCL16 stimulated proliferation and chemotaxis of HUVEC in a dose-dependent manner, reaching a maximum at 1 nM. CXCL16 also significantly induced tube formation of HUVEC on Matrigel. Further, exposure of HUVEC to CXCL16 led to a time- and dose-dependent activation of mitogen-activated protein kinase (ERK1/2), which was completely inhibited by a mitogen-activated protein kinase kinase inhibitor, PD98059. Proliferation and tube formation in response to CXCL16 were also blocked by the pretreatment with PD98059, but not CXCL16-induced chemotaxis. Thus, our data indicate that CXCL16 may act as a novel angiogenic factor for HUVEC and that ERK is involved as an important signaling molecule to mediate its angiogenic effects.

Keywords: CXCL16; Angiogenesis; Endothelial cell

Angiogenesis, the formation of new blood vessels from pre-existing endothelium, is a fundamental step in a variety of physiological and pathological conditions including wound healing, embryonic development, chronic inflammation, and tumor growth [1–3]. The process of angiogenesis is complex and involves several discrete steps, such as extracellular matrix degradation, proliferation, migration, and morphological differentiation of endothelial cells to form tubes [4]. The angiogenic process is tightly controlled by a wide variety of positive or negative regulators, and many of these factors are initially characterized in other biological activities.

CXCL16 was identified as a chemokine produced from dendritic cells, which attracts T cells in lymphoid organ [5,6]. We independently cloned this molecule as a scavenger receptor that binds phosphatidylserine and oxidized lipoprotein (SR-PSOX) [7], and showed that this molecule is expressed by macrophages in vitro and in atherosclerotic lesions in vivo [7,8]. It is also involved in the massive accumulation of cellular cholesterol during the generation of macrophage foam cells associated with atherosclerotic lesion development [9]. In addition to macrophages, Hofnagel et al. [10] have demonstrated CXCL16 expression in cultured aortic smooth muscle cells (ASMC) by RT-PCR. More recently, it has been reported that human ASMC express CXCR6, and that CXCL16 increases cell–cell adhesion and ASMC proliferation [11]. We recently found that CXCL16 was strongly expressed in valvular and neocapillary endothelial cells in patients with infective endocarditis, rheumatic, and atherosclerotic valvular disease [12]. These data indicate that CXCL16 can also be involved in proliferation and migration of endothelial cells. Accordingly, we asked whether CXCL16 might act as a novel angiogenic stimulus directly involved in the processes of angiogenesis.

In the present study, we investigated the angiogenic activity of CXCL16 for endothelial cells. We also examined the signaling cascades involved in CXCL16-mediated angiogenic effects in human umbilical vein endothelial cells (HUVEC) in vitro.

* Corresponding author. Fax: +81 75 751 3463.
E-mail address: harai@kuhp.kyoto-u.ac.jp (H. Arai).
[1] These authors equally contributed to this work.

0006-291X/$ - see front matter © 2005 Elsevier Inc. All rights reserved.
doi:10.1016/j.bbrc.2005.03.200

Materials and methods

Materials. A mitogen-activated protein kinase kinase (MEK) inhibitor, PD98059, was obtained from Calbiochem (San Diego, CA). Recombinant human CXCL16 was from R&D Systems (Minneapolis, MN). bFGF was from Kurabo (Osaka, Japan).

Cell culture. HUVEC were purchased from Kurabo and grown in HuMedia EG2 (Kurabo) culture medium. Cells were maintained at 37 °C in 5% CO_2 and 95% ambient air. Experiments were performed with cells in 3–6 passages.

Cell proliferation assay. Cell proliferation was examined using WST-1. WST-1 assay is based on formazon dye formation, which directly correlates with the number of metabolically active cells in the culture. 6×10^3 cells grown in a 96-well plate for 24 h were partially starved in Humedia EB2 supplemented with 1% FBS for 24 h and then stimulated by CXCL16 for another 48 h. In some cases, cells were pretreated with PD98059 (25 μM) for 30 min before stimulation. Ten microliters of WST-1 solution (Takara, Japan) was added to each well and incubated for 3 h, and absorbencies at 450 nm of the medium were measured using a microplate reader (Bio-Rad, Model 550, Tokyo, Japan).

Chemotaxis assay. The chemotactic motility was assessed using a modified Boyden chamber with a 5 μm-pore polycarbonate filter (Neuro Probe, Gaithersburg, MD). Cells were starved in Humedia EB2 with 1% FBS for overnight before assays. Fresh 0.5% BSA Humedia EB2 containing CXCL16 was placed in the lower wells. Trypsin-harvested cells were suspended at a final concentration of 5×10^5/ml in Humedia EB2 containing 0.5% BSA. PD98059 was given to the cells for 30 min at room temperature before seeding. Fifty microliters of the cell suspension was loaded into each upper well and the chamber was then incubated at 37 °C for 4 h. Non-migrating cells on the upper surface of the filter were removed by rubber swab. Filters were fixed and stained with Diff-Quik solution (International Reagents, Kobe, Japan). Cell motility was quantified by counting cells that migrated across the filter toward the lower surface in three fields per filter under optical microscope at 100× magnification.

Tube formation assay. The tube formation assay was performed as previously described [13]. Briefly, 250 μl of growth factor-reduced Matrigel (BD Biosciences Discovery Labware, Bedford, MA) was added per well of a 24-well plate and allowed to polymerize at 37 °C for at least 30 min. Trypsin-harvested cells (5×10^4) suspended in 250 μl of Humedia EB2 containing CXCL16 or bFGF were seeded onto Matrigel. PD98059 was given to the cells for 30 min at room temperature before seeding. After incubation for 24 h at 37 °C, capillary-like structures within the Matrigel layer were stained with calcein (Molecular Probes, Eugene, OR) and photographed under fluorescent microscope. Total tube length was quantified using image analysis software of Image-Pro Plus (version 3.0; Media Cybernetics, Baltimore, MD).

Immunoprecipitation and Western blotting. HUVEC were incubated in Humedia EB2 with 1% FBS overnight before stimulated with CXCL16. In some cases, cells were pretreated with PD98059 (25 or 50 μM) for 30 min before stimulated by CXCL16. ERK activation was measured by p44/42 MAP Kinase Assay Kit (Cell Signaling Technology, Beverly, MA). Briefly, the cell lysate was collected by ice-cold cell lysis buffer provided by the kit. Immunoprecipitation was done by using immobilized phospho-p44/42 MAP kinase (Thr202/Tyr204) monoclonal antibody. The precipitate is then incubated with Elk-1 fusion protein to active ERK to phosphorylate Elk-1. Subsequently, protein from each sample was loaded onto a sodium dodecyl sulfate 12% polyacrylamide gel and transferred onto a PVDF membrane. The blocked membranes were then incubated with rabbit anti-phospho-Elk-1 antibody (1:1000). Immunoreactive bands were visualized using detection reagents.

Statistical analysis. Data are expressed as means ± SD. Statistical analyses were performed by using one-way ANOVA followed by Dunnett's test to evaluate statistical significance between two groups. p values less than 0.05 were considered statistically significant.

Results and discussion

CXCL16 induces proliferation, migration, and tube formation of HUVEC

To determine whether CXCL16 can induce angiogenesis in endothelial cells, the ability of CXCL16 as an angiogenic stimulus has been assessed in in vitro angiogenesis models. We first examined the effect of CXCL16 on HUVEC proliferation by WST-1 assay. Incubation of the cells with CXCL16 for 48 h resulted in an increase of HUVEC in a dose-dependent manner significantly from 0.1 to 10 nM and the cell number reached a plateau at 1 nM (Fig. 1A). CXCL16 (1 nM) increased the cell number by approximately 35% over the control. We then compared the effect of CXCL16 with that of basic fibroblast growth factor (bFGF) (10 ng/ml), which is known to stimulate HUVEC proliferation (Fig. 1B), and found that the effect of CXCL16 on endothelial proliferation was less potent than that of bFGF. CXCL16 is also shown to induce ASMC proliferation at 5 nM [11]. Therefore, the effect of CXCL16 on endothelial proliferation is consistent with the effect on other cell type. We next determined the effect of CXCL16 on chemotactic motility of HUVEC by modified Boyden chamber assay (Figs. 1C and D). CXCL16 stimulated the chemotactic motility of HUVEC in a dose-dependent manner. The chemotactic motility at 1 nM CXCL16 was 1.4-fold over the control. This effect of CXCL16 was also less potent than that of bFGF.

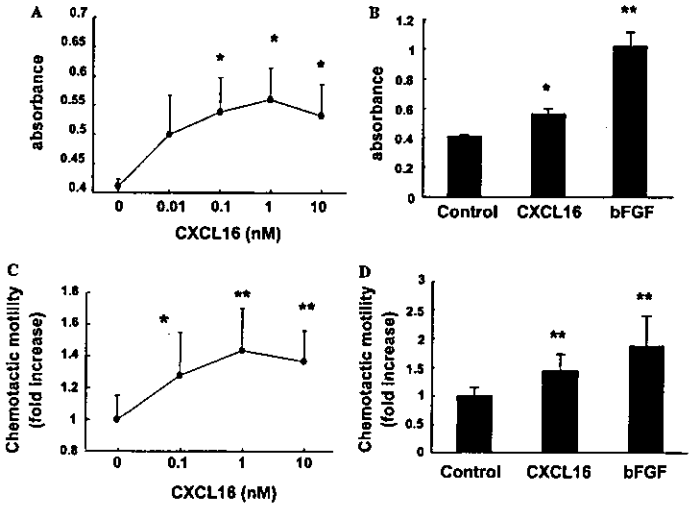

Fig. 1. CXCL16-induced proliferation and migration in HUVEC. (A) After HUVEC were cultured with the indicated concentrations of CXCL16 for 48 h, cell proliferation was determined by WST-1 assay ($n = 7$). (B) Effects of CXCL16 and bFGF on HUVEC proliferation. Cells were stimulated with 1 nM CXCL16 or 10 ng/ml bFGF for 48 h and cell proliferation was determined by WST-1 assay ($n = 7$). (C) CXCL16-induced chemotaxis in HUVEC. HUVEC were placed in the upper chamber, and the various concentrations of CXCL16 were added in the lower chamber. Cell migration was assayed by modified Boyden chamber assay ($n = 9$). (D) Effects of CXCL16 and bFGF on chemotaxis of HUVEC ($n = 9$). EB2 (0.5% BSA) with 1 nM CXCL16 or 20 ng/ml bFGF was placed in the lower wells. After 4 h, chemotactic motility of HUVEC was measured as described under Materials and methods. Data A and B represent means ± SD, and similar results were obtained in three independent experiments. Data C and D are expressed as fold increase over control ± SD from three independent experiments with triplicate determinations. $^{*}p < 0.05$; $^{**}p < 0.01$ vs. control.

The effect of CXCL16 on the morphological differentiation of HUVEC into vascular structures in vitro was investigated using Matrigel tube formation assay. When placed on growth factor-reduced Matrigel in the absence of angiogenic factors, HUVEC did not form complete tube-like structures. However, by adding 1 nM of CXCL16, we could observe the networks similar to those formed by bFGF, which consisted of a large number of cells (Fig. 2A). By measuring the length of tube in the tube network using an image analysis program, CXCL16 (1 nM) stimulated tube formation by 1.5-fold over the control (Fig. 2B). In addition, CXCL16 stimulated the tube formation in a dose-dependent manner with a significant increase from 0.0 1 to 10 nM (data not shown). These results indicate that CXCL16 has a novel angiogenic activity in in vitro human endothelial cell culture system. However, these effects of CXCL16 were weaker than those of bFGF.

CXCL16 activates ERKs in HUVEC

Recent studies have shown that activation of ERK is closely involved in proliferation, migration, or morphogenesis of endothelial cells induced by various angiogenic factors [13–17]. Therefore, we examined whether CXCL16 can stimulate ERK in HUVEC. Subconfluent HUVEC were exposed to various concentrations of CXCL16, and the activation of ERK was analyzed by immunoprecipitation and Western blot analysis as described under Materials and methods. As shown in Figs. 3A and B, CXCL16 induced the phosphorylation of Elk-1 in a dose- and time-dependent manner. The phosphorylation peaked at 10 min after stimulation with CXCL16 and declined thereafter. We then checked the effect of a specific MEK inhibitor, PD98059, on ERK activation by CXCL16 by adding the inhibitor 30 min before stimulation with CXCL16. As expected, pretreatment with PD98059 abolished CXCL16-induced ERK activation both at 25 and 50 μM (Fig. 3C).

ERK activation is involved in CXCL16-mediated angiogenesis in HUVEC

The activation of the ERK pathway by CXCL16 prompted us to determine whether this biochemical

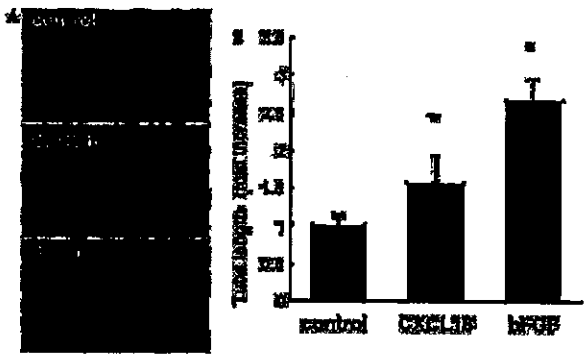

Fig. 2. CXCL16-induced tube formation of HUVEC. HUVEC were plated on Matrigel-coated wells with media alone, 1 nM CXCL16, or 20 ng/ml bFGF (A). After 20 h, the tubes were visualized using calcein staining and photographs were taken under microscope (40×). Shown is a representative picture from three independent experiments. (B) The length of tube was quantitated using Image-Pro Plus software. Data are expressed as fold increase over control and means ± SD from five independent experiments with triplicate determinations. $^{*}p < 0.01$ vs. control.

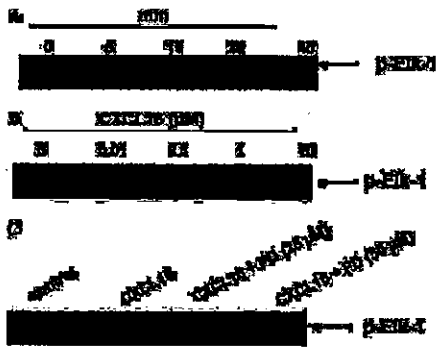

Fig. 3. CXCL16-induced ERK activation was blocked by PD98059 in HUVEC. (A) Time course of CXCL16-induced ERK activation. HUVEC were stimulated with 1 nM CXCL16 for the indicated times. Activation of ERK was determined as described under Materials and methods. Shown is a representative Western blot from three independent experiments. (B) Dose-dependent ERK activation. HUVEC were stimulated with various concentrations of CXCL16 for 10 min. Shown is a representative Western blot from three independent experiments. (C) HUVEC were pretreated with PD98059 (25 and 50 μM) for 30 min and stimulated with 1 nM CXCL16 for 10 min. Shown is a representative Western blot from three independent experiments.

event is important for angiogenic activities of CXCL16 in HUVEC. First, we tested the effect of PD98059 on CXCL16-induced HUVEC proliferation. As shown in Fig. 4A, pretreatment of the cells with PD98059 (25 μM) completely inhibited CXCL16-induced HUVEC proliferation, suggesting that ERK is closely involved in CXCL16-induced endothelial cell proliferation.

It has been reported that ERK is required for endothelial cell chemotaxis stimulated by bFGF and the placental angiogenic hormone proliferin [17,18]. In contrast, VEGF-induced HUVEC migration is reported to be independent of ERK [19]. Therefore, we next examined the effect of PD98059 on CXCL16-induced chemotaxis in HUVEC. As shown in Fig. 4B, PD98059 had no significant effect on CXCL16-induced cell motility, even though the same concentrations of PD98059 blocked CXCL16-induced ERK activation (Fig. 3C). These results do not indicate that CXCL16-induced chemotaxis is mediated by ERK. Although the present study could not identify the signaling mechanisms of CXCL16-induced chemotaxis, our data did not show that activation of ERK by CXCL16 is required for the chemotactic effect in HUVEC.

Finally, we examined the signaling mechanism of CXCL16-induced tube formation in HUVEC. PD98059 (25 μM) preteatment markedly inhibited tube formation induced by CXCL16 in HUVEC (Fig. 5), suggesting that G protein-dependent activation of the ERK pathway is critically involved in promoting morphological differentiation of endothelial cells on Matrigel.

In this report, we demonstrate that CXCL16 has a novel function as an angiogenic factor for endothelial cells. In in vitro angiogenesis models, we have revealed that the stimulation of HUVEC with CXCL16 leads to an increase in cell proliferation as well as chemotactic motility, and strongly induces the formation of tube network. Our data also showed that ERK signaling is involved in cell proliferation and tube formation induced by CXCL16 in HUVEC.